



LJMU Research Online

Turnewitsch, R, Dumont, M, Kiriakoulakis, K, Legg, S, Mohn, C, Peine, F and Wolff, G

Tidal influence on particulate organic carbon export fluxes around a tall seamount

<http://researchonline.ljmu.ac.uk/id/eprint/6285/>

Article

Citation (please note it is advisable to refer to the publisher's version if you intend to cite from this work)

Turnewitsch, R, Dumont, M, Kiriakoulakis, K, Legg, S, Mohn, C, Peine, F and Wolff, G (2016) Tidal influence on particulate organic carbon export fluxes around a tall seamount. Progress in Oceanography, 149. pp. 189-213. ISSN 0079-6611

LJMU has developed [LJMU Research Online](http://researchonline.ljmu.ac.uk/) for users to access the research output of the University more effectively. Copyright © and Moral Rights for the papers on this site are retained by the individual authors and/or other copyright owners. Users may download and/or print one copy of any article(s) in LJMU Research Online to facilitate their private study or for non-commercial research. You may not engage in further distribution of the material or use it for any profit-making activities or any commercial gain.

The version presented here may differ from the published version or from the version of the record. Please see the repository URL above for details on accessing the published version and note that access may require a subscription.

For more information please contact researchonline@ljmu.ac.uk

<http://researchonline.ljmu.ac.uk/>

1 **Tidal influence on particulate organic carbon export fluxes around a tall seamount**

2

3 **Robert Turnewitsch ¹, Matthew Dumont ^{1,2}, Kostas Kiriakoulakis ³, Sonya Legg ⁴, Christian Mohn ⁵, Florian**
4 **Peine ⁶, George Wolff ⁷**

5

6 **¹ Scottish Association for Marine Science, Oban PA37 1QA, UK**

7 **² University of Edinburgh, School of Geosciences, Grant Institute, The King's Buildings, James Hutton**
8 **Road, Edinburgh, EH9 3FE, UK**

9 **³ Liverpool John Moores University, Byrom St., Liverpool L3 3AF, UK**

10 **⁴ Princeton University, Atmospheric and Oceanic Sciences, 300 Forrestal Road, Sayre Hall, Princeton, NJ**
11 **08544, USA**

12 **⁵ Aarhus University, Department of Bioscience - Applied Marine Ecology and Modelling, Frederiksborgvej**
13 **399, 4000 Roskilde, Denmark**

14 **⁶ University of Rostock, Institute for Biosciences - Marine Biology, Albert-Einstein-St. 3, 18059 Rostock,**
15 **Germany**

16 **⁷ University of Liverpool, Department of Earth & Ocean Sciences, Liverpool L69 3GP, UK**

17

18

19 **Corresponding author: Robert Turnewitsch: robert.turnewitsch@sams.ac.uk**

20 **Keywords: seamount, tide, particulate organic carbon export, Cape Verde**

21

22

23 **ABSTRACT**

24 As tall seamounts may be 'stepping stones' for dispersion and migration of deep open ocean fauna, an
25 improved understanding of the productivity at and food supply to such systems needs to be formed. Here,
26 the $^{234}\text{Th}/^{238}\text{U}$ approach for tracing settling particulate matter was applied to Senghor Seamount --- a tall
27 sub-marine mountain near the tropical Cape Verde archipelago --- in order to elucidate the effects of
28 topographically-influenced physical flow regimes on the export flux of particulate organic carbon (POC)
29 from the near-surface (topmost ≤ 100 meters) into deeper waters. The comparison of a suitable reference
30 site and the seamount sites revealed that POC export at the seamount sites was ~2-4 times higher than at
31 the reference site. For three out of five seamount sites, the calculated POC export fluxes are likely to be
32 underestimates. If this is taken into account, it can be concluded that POC export fluxes increase while the
33 passing waters are advected around and over the seamount, with the highest export fluxes occurring on
34 the downstream side of the seamount. This supports the view that biogeochemical and biological effects of
35 tall seamounts in surface-ocean waters might be strongest at some downstream distance from, rather than
36 centred around, the seamount summit. Based on measured (vessel-mounted ADCP) and modelled (regional
37 flow field: AVISO; internal tides at Senghor: MITgcm) flow dynamics, it is proposed that tidally generated
38 internal waves result in a 'screen' of increased rates of energy dissipation that runs across the seamount
39 and leads to a combination of two factors that caused the increased POC export above the seamount:
40 (1) sudden increased upward transport of nutrients into the euphotic zone, driving brief pulses of primary
41 production of new particulate matter, followed by the particles' export into deeper waters; and (2) pulses
42 of increased shear-driven aggregation of smaller, slower-settling into larger, faster-settling particles. This
43 study shows that, under certain conditions, there can be an effect of a tall seamount on aspects of surface-
44 ocean biogeochemistry, with tidal dynamics playing a prominent role. It is speculated that these effects can
45 control the spatiotemporal distribution of magnitude and nutritional quality of the flux of food particles to
46 the benthic and benthic-pelagic communities at and near tall seamounts.

47

49 **1. INTRODUCTION**

50 A fraction of the biogenic particulate matter that is photoautotrophically produced in the upper sunlit
51 layers of the ocean settles into deeper waters and constitutes food for heterotrophic organisms in the
52 deeper waters and the seafloor. Often this downward 'export' of biogenic particulate matter from the
53 topmost 10s or 100s of meters of the water column is quantified in terms of the export of particulate
54 organic carbon (POC). On large quasi-horizontal scales on the order of 1000s of kilometers, the combination
55 of basin-scale current distribution and latitudinally dependent insolation indirectly control the distribution
56 of primary productivity and POC export (e.g., Lutz et al., 2007; Watling et al., 2013). On quasi-horizontal
57 scales on the order of 10s to 100s of kilometers, physical-oceanographic features such as mesoscale eddies
58 and fronts are known to influence POC export (e.g., Buesseler et al., 2008; Resplandy et al., 2012). Islands
59 and island chains have also been shown to influence POC export through their influence on regional and
60 local flow dynamics (e.g., Bidigare et al., 2003; Morris et al., 2007; Maiti et al., 2008; Verdeny et al., 2008).
61 By contrast, very little is known about the influence of submarine mountains. Seamounts are often defined
62 as tall (> 1000 m from base to summit), relatively isolated submarine features, of which there are estimated
63 to be well over 100000 across the ocean (Wessel et al., 2010). About 2000 seamounts are thought to be at
64 least 3000 m high, with the vast majority reaching water depths of ≤ 100 m.

65 Seamounts interact in systematic and complex ways with different flow components of ocean currents,
66 including quasi-steady and oscillating ones (see, for example, reviews by White and Mohn, 2004; Lavelle
67 and Mohn, 2010; Turnewitsch et al., 2013). As tall seamounts may be 'stepping stones' for dispersion and
68 migration of deep open ocean fauna (Rowden et al., 2010), an improved understanding of the productivity
69 and food supply to such systems needs to be formed. It has been argued that the fluid dynamics at
70 seamounts that reach into the near-surface ocean could have a significant effect on local or regional water
71 column biogeochemistry (Goldner and Chapman, 1997; Mullineau and Mills, 1997; Mohn and White, 2010).
72 This could lead to seamounts acting as hotspots of high productivity and potentially high POC-export, at
73 least in oligotrophic regions, a phenomenon described as the 'seamount'- or 'classic'- hypothesis (Dower

74 and Mackas, 1996). Observed enhancements of primary production around seamounts have been
75 attributed to a greater local upward mixing of deep, nutrient-replete waters (Rogers, 1994; Mouriño et al.,
76 2000). However, as noted by Genin (2004), upwelling is unlikely to be a permanent feature and any
77 enhancement of primary production might only be realised downstream of the seamount. Rowden et al.
78 (2010) also argue that the paradigm that tall seamounts “have high production supported by localized
79 bottom-up forcing, [is] not supported by the weight of existing evidence”.

80 This paper presents the first case study in which the distribution of export of POC from the surface
81 waters near and over a tall seamount was investigated. For the particular situation at the time of the study,
82 the three main objectives were (O1) to identify the predominant physical-oceanographic features at and
83 near the seamount; (O2) to establish how POC export is distributed at the seamount compared to
84 reference stations; and (O3) to scrutinize the results of O1 and O2 for a seamount effect on POC export.
85 The core hypothesis is that a tall seamount can trigger enhanced localised POC export. The findings of this
86 study illustrate the importance of the physical-oceanographic complexity that results from regional
87 ‘background’ variability and seamount-controlled flow / topography interactions for an understanding of
88 biogeochemical processes at tall seamounts. The results indicate that, in the case of Senghor Seamount,
89 tidally generated internal waves are likely to have led to an abrupt and localised enhancement of POC
90 export, with this biogeochemical signal being advected downstream and away from the seamount.

91

92

93

94 **2. MATERIAL AND METHODS**

95

96 **2.1 Environmental setting**

97 The study was carried out at Senghor Seamount, a large, approximately conical feature on the Cape
98 Verde Rise, centred at ~17.2°N, 21.9°W and ~ 110 km north-east of Sal Island of the Cape Verde archipelago
99 and ~ 550 km west of the coast of Senegal (Fig. 1). The summit plateau is at ~ 105 m depth whereas the rise
100 is at ~ 3200 m. The summit plateau has a maximum extent of ~ 5 km; at the base the seamount has an

101 approximate diameter of 35 km. The seamount is situated amongst several well-studied oceanographic
102 features, including the Cape Verde Frontal Zone (CVFZ; Zenk et al., 1991) to the north (N) and northwest
103 (NW) (Fig. 1), the Mauritanian Upwelling Zone (Mittelstaedt, 1983) to the northeast (NE), and the Guinea
104 Dome (Siedler and Zangenberg, 1992) and Shadow Zone (Luyten et al., 1983) to the south (S).

105 Current-flow data derived from nearby moorings (Müller and Siedler, 1992; Vangriesheim et al., 2003),
106 Acoustic Doppler Current Profiler (ADCP) transects (Stramma et al., 2008), and satellite-altimetry-forced
107 models (Lazaro et al., 2005) suggest that at depths shallower than ~ 800 m mean residual flow in the region
108 is to the southwest (SW) at $\sim 0.05 - 0.1 \text{ m s}^{-1}$ which is consistent with the general direction of the North
109 Equatorial Current (NEC) (Fig. 1). At depths greater than ~ 800 m, residual flow is to the south at only
110 $0.005 - 0.01 \text{ m s}^{-1}$. Important sources of variability that are superimposed onto this mean residual flow are
111 the seasonal migration of the wind-stress curl with the inter-tropical convergence zone (ITCZ) (Stramma
112 and Siedler, 1988; Lázaró et al., 2005), baroclinic instabilities originating from the CVFZ), barotropic tidal
113 oscillations (Siedler and Paul, 1991), and internal (baroclinic) tides (Siedler and Paul, 1991; Arbic et al.,
114 2012).

115 Although the centre of the Mauritanian Upwelling Zone is located off Cape Blanc, i.e., well to the NE of
116 Senghor Seamount, filaments of upwelled water have been observed to extend out westward driven by
117 trade-winds and meso-scale eddies (Mittelstaedt, 1983; Pastor et al., 2008; Meunier et al., 2012). The
118 filaments tend not to extend southward towards Senghor Seamount though. Nevertheless, satellite remote
119 sensing data from MODIS-Aqua (acquired from giovanni.gsfc.nasa.gov) will be utilised to evaluate the
120 extent of eutrophic waters during this study.

121 Primary production typically peaks in the first quarter of the year, following the wind stress maximum
122 (Lathuiliere et al., 2008; Ohde and Siegel, 2010); but spatially- and temporally-sporadic peaks in
123 productivity have been observed later between April and June, and it has been speculated that they occur
124 in association with dust deposition from the Sahara and Sahel regions (Ratmeyer et al., 1999b; Fitzsimmons
125 et al., 2013). However, dust deposition in summer has been noted to be five-times lower than in December
126 and January (Chiapello and Bergametti, 1995); and, using a remotely sensed optical aerosol depth index
127 and chlorophyll-*a* concentration as proxies for dust deposition and productivity, respectively, Ohde and

128 Siegel (2010) reported that the input of Saharan dust accounts for just 5% of the variability in observed
129 chlorophyll-*a* concentrations. By contrast, there is some evidence to suggest that large amounts of dust
130 particles that are incorporated into marine-snow aggregates could lead to increased mass densities of
131 these aggregates and, as a consequence, higher settling speeds and POC export (e.g., Fischer et al., 2016).

132

133 **2.2 The $^{234}\text{Th}/^{238}\text{U}$ approach to estimate POC export**

134 The use of the thorium-234 / uranium-238 ($^{234}\text{Th} / ^{238}\text{U}$) pair of naturally occurring radionuclides to
135 measure export flux is made possible due to the contrasting adsorption behaviours of the two elements
136 (Bhat et al., 1968; Coale and Bruland, 1985, 1987; Buesseler, 1998). In oxygenated seawater the very long-
137 lived ^{238}U (half life: $t_{1/2} \approx 4.468$ billion years) behaves chemically conservative and is removed only by alpha-
138 decay to its daughter, ^{234}Th . If unperturbed, the two radionuclides remain in so-called radioactive
139 equilibrium: i.e., over negligibly-short time scales relative to the half-life of ^{238}U , the rate of decay of ^{234}Th is
140 matched by the rate of decay of ^{238}U . However, in seawater Th is highly particle reactive (e.g., Santschi et
141 al., 2006) and readily scavenged by adsorption onto particle surfaces, with an affinity for acid
142 polysaccharides (Guo et al., 2002; Alvarado Quiroz et al., 2006; Buesseler et al., 2006). Most research so far
143 suggests that larger, more rapidly-settling particles play the dominant role in the export of POC into the
144 *deep interior* ocean (e.g. McCave, 1975; Clegg and Whitfield, 1990,1991; Ducklow et al., 2001; De La Rocha
145 and Passow, 2007) (in the topmost few hundred meters of the water column smaller slowly-settling
146 particles can also contribute significantly to the downward flux of particulate matter, but only into the
147 shallower twilight zone; e.g., Alonso-González et al., 2010). On these settling particles, the adsorbed ^{234}Th is
148 transported downwards and 'exported' from its original parcel of water. If the rates of adsorption and
149 settling are high in comparison to the production rate of ^{234}Th , a radioactive disequilibrium between ^{238}U
150 and ^{234}Th forms, i.e., the radioactivity of ^{238}U is higher than the radioactivity of ^{234}Th . This disequilibrium can
151 be used as a measure of the intensity of the export flux of ^{234}Th from a given parcel of water. If the ratio of
152 POC to ^{234}Th is known for the settling particles, the ^{234}Th export flux can be converted into a POC export
153 flux. Due to the short half-life of ^{234}Th ($t_{1/2} = 24.1$ d) it captures the characteristic time scales of many bio-
154 oceanographic processes such as phytoplankton blooms (Buesseler et al., 2006; Passow et al., 2006).

155

156 2.2.1 Sampling

157 Samples were collected during cruise M79/3 of R/V Meteor (24/09 - 22/10/2009; Christiansen et al.,
158 2011). A map of sampling sites around the seamount along with two additional far-field stations north (N-
159 Ref) and south (S-Ref) of the seamount is shown in Fig. 1. Water samples for total (dissolved + particulate)
160 ^{234}Th were collected with a 22-bottle Seabird-Systems CTD-rosette (SBE 911plus) equipped with a Winkler-
161 calibrated dissolved-oxygen (DO) probe. Within the topmost 100 m 5-8 depths were sampled for total ^{234}Th
162 (S-Slope: 5 depth levels; Summit, W-Slope, N-Slope, E-Slope, S-Ref: 6 depth levels; N-Ref: 8 depth levels)
163 (Tab. 1).

164 To collect samples for POC and ^{234}Th in particulate matter, up to two large-volume stand-alone pumping
165 systems (SAPS; Challenger Oceanic) were deployed at the aforementioned CTD stations (Tab. 1). The SAPS
166 filtered between 381 and 1634 litres of water through a 293 mm-diameter, acid-washed 53 μm nylon mesh
167 before two sequentially-stacked pre-ashed glass fibre GF/F filters with a nominal pore-size of 0.7 μm . The
168 second GF/F filter was used to correct for what is thought to be adsorption of dissolved organic carbon
169 (DOC) (Turnewitsch et al., 2007) and dissolved ^{234}Th onto the GF/F filters. Material collected on the mesh
170 and the filters was analysed for organic carbon and ^{234}Th (see Section 2.2.2 below). This approach thus
171 differentiated POC and ^{234}Th in operationally defined nominal particle-size fractions of 0.7 – 53 μm and
172 > 53 μm .

173

174 2.2.2 Laboratory and analytical procedures

175 2.2.2.1 Total ^{234}Th

176 Total ^{234}Th analysis was carried out on the bottle-collected water samples, applying the procedures
177 outlined by Rutgers van der Loeff and Moore (1999), Turnewitsch and Springer (2001) and Turnewitsch et
178 al. (2008) with slight modifications and taking into account the review of Rutgers van der Loeff et al. (2006).
179 Sample processing involved co-precipitating thorium in the unfiltered samples with MnO_2 . To form MnO_2 ,
180 150 μL of 25% NH_3 solution, 100 μL of KMnO_4 solution (60 g L^{-1}) and 40 μL of $\text{MnCl}_2 \bullet 4\text{H}_2\text{O}$ solution
181 (400 g L^{-1}) were added successively to each sample. The processed water volume was of intermediate size

182 for this kind of analysis (average \pm one standard deviation (1SD): 7.772 ± 0.716 L). The precipitating MnO_2
183 particles were left to grow for between ~ 6 and ~ 12 hr. The MnO_2 -containing water was then filtered at
184 400 mbar overpressure through 142-mm-diameter polycarbonate filters with $1.0 \mu\text{m}$ nominal pore width to
185 collect the precipitate and natural particles. This step of the procedure separates thorium from its dissolved
186 uranium parent. Following filtration, the polycarbonate filters were air dried, folded in a reproducible way,
187 and wrapped in Mylar foil before being placed into a beta counter.

188 Beta counting was performed using three identical Risø GM25-5A multiscalers: one aboard R/V
189 Meteor, one at the University of Rostock and another at the Scottish Association for Marine Science
190 (SAMS). Each multiscaler has 5 detectors and the 15 detectors that were used were intercalibrated with
191 standard filters that carry a known ^{238}U radioactivity in equilibrium with ^{234}Th (Turnewitsch and Springer,
192 2001; Turnewitsch et al., 2008). This intercalibration also yielded the counting efficiencies for the 15
193 detectors. Counting efficiencies ranged from 28% up to 33% with absolute errors (given as 1SD) ranging
194 from $\pm 1\%$ to $\pm 1.74\%$. Each sample was measured on board as soon as possible after sample processing
195 and then again at least three times over a period of ten months (approximately twelve ^{234}Th half-lives).
196 Repeat measurements ensure that the shape of the decay curve can be scrutinised for signs of
197 contamination (Peine et al., 2009) and that a robust background can be determined. Mean \pm 1SD
198 background activities were 0.50 ± 0.12 counts per minute (cpm).

199 To estimate total ^{234}Th activities (expressed as disintegrations per minute (dpm) per litre of in situ
200 seawater: dpm L^{-1}) a correction for in-growth from ^{238}U decay between sampling and filtration was applied.
201 Another correction includes the decay-related loss of ^{234}Th between filtration and the first activity
202 measurement. ^{238}U activities in dpm L^{-1} were derived from the relationship with salinity as described by
203 Chen et al. (1986) and re-evaluated by Owens et al. (2011). Overall uncertainties for total ^{234}Th activities are
204 reported as \pm 1SD and resulted from error propagations, taking into account uncertainties in in situ mass
205 density of sampled waters, intercalibration, counting statistics, estimate of the activity at the time of
206 sampling (corrections for ^{234}Th decay and ingrowth), counting efficiency, filtered volume, and ^{238}U activity
207 (Turnewitsch et al., 2008).

208 On previous cruises, a second precipitation was conducted on selected samples to directly determine
209 the extraction efficiency, and, for total ^{234}Th , extraction efficiencies were found to be $99.0 \pm 1.4\%$ which is
210 analytically indistinguishable from the $98 \pm 3\%$ reported independently by LeMoigne et al. (2013). There is
211 growing evidence that even waters from the interior ocean (i.e., away from ocean boundaries) may contain
212 detectable disequilibria (e.g., Owens et al., 2015). However, replicate sampling ($N = 5$) at ~ 1400 m water
213 depth (1894 meters above bottom (mab)) at N-Ref revealed an average $\pm 1\text{SD}$ total ^{234}Th activity of
214 2.37 ± 0.13 dpm L^{-1} (relative uncertainty of $\pm 5.5\%$) which is analytically indistinguishable from the salinity-
215 derived ^{238}U activity of 2.44 ± 0.05 dpm L^{-1} and indicates the $^{234}\text{Th} / ^{238}\text{U}$ pair was in fact in radioactive
216 equilibrium at this location and depth. This demonstrates within analytical uncertainties the quantitative
217 recovery of thorium from the seawater samples for this intermediate-volume technique and is in
218 agreement with a number of previous studies (e.g., Morris et al., 2007; Lampitt et al., 2008; Turnewitsch et
219 al., 2008; LeMoigne et al., 2013).

220

221 **2.2.2.2 Particulate ^{234}Th , particulate organic carbon (POC) and particulate nitrogen (PN)**

222 For particulate ^{234}Th , SAPS samples were processed following the approach described by Morris et al.
223 (2007), with slight modifications. For POC and PN, procedures followed Turnewitsch et al. (2007), with
224 slight modifications. In summary, particles collected on the $53 \mu\text{m}$ nylon mesh were rinsed with purified
225 water into a graduated cylinder. The sample was then gently stirred to homogenise the particles in
226 suspension. While still swirling, the suspension was split: one split of known volume was immediately
227 filtered onto 25 mm diameter pre-ashed GF/F filters that were then stored frozen until POC and PN
228 analysis; the other split of known volume was immediately filtered through a $0.4 \mu\text{m}$ nominal pore width
229 142 mm-diameter polycarbonate filter that was air-dried, folded and wrapped in Mylar foil in a
230 reproducible manner for particulate ^{234}Th analysis. Exposure of the particles to the purified water was
231 limited to a few minutes. For the smaller particle size fraction ($0.7 - 53 \mu\text{m}$), four 24 mm diameter disk sub-
232 samples were taken from each of the 293 mm diameter pre-ashed GF/F filters which were then air-dried in
233 preparation for direct beta-counting as described above. Corresponding GF/F-filter sub-samples for POC
234 and PN were stored frozen for later analysis.

235 Counting efficiencies for the folded polycarbonate filters that carry the > 53 μm particles were
236 determined with standard filters as described above. As the GF/F filter sub-samples have similar mass
237 density and diameter (and thus similar absorption properties) compared to the QMA-filter sub-samples
238 that we used as part of the GEOTRACES ^{234}Th intercalibration (Maiti et al., 2012), the counting efficiency of
239 $43 \pm 2\%$ that was determined for the QMA filter disks was applied to the filter sub-samples of this study.
240 Activities on the first GF/F filter were corrected based on activities on the second GF/F filter, assuming that
241 activities on the second filter represent the combination of activity due to ^{234}Th that adsorbed from the
242 dissolved phase onto the filter and activity from the background of comparatively long-lived beta-emitters
243 (Benitez-Nelson et al., 2001a). Activities were corrected for ^{234}Th decay between sampling and the first
244 measurement.

245 The analytical method to determine POC and PN was similar to that performed by Kiriakoulakis et al.
246 (2009). In short, SAPS filter sub-samples for both particle size fractions were decarbonated for POC analysis
247 (Yamamouro and Kayanne, 1995), whilst PN analysis was carried out on non-decarbonated subsamples.
248 Analysis was then carried out using a CEInstruments NC 2500 CHN analyser with quadruplicates. Adsorption
249 of dissolved organic matter (DOM) onto the GF/F filters was corrected for by subtracting the values
250 obtained for the second in-line filter from values that were obtained for the first filter (Turnewitsch et al.,
251 2007).

252 Calculations of final particulate- ^{234}Th activity and final POC and PN concentrations took into account
253 corrections for the split volume and scaling-up to full effective filter areas of the 293 mm-diameter filters
254 and filtered volumes.

255

256 **2.3 Physical oceanography**

257 Information on hydrography and flow dynamics around the upper parts of the seamount was derived
258 from the CTD casts, vessel-mounted ADCP (VM-ADCP) measurements and numerical modelling. Due to a
259 technical defect, CTD data from stations with station numbers higher than 911 (with the exception of 920
260 and 951) are incomplete or not readable. Water samples could still be collected reliably though. On-station
261 and underway VM-ADCP data were collected across Senghor Seamount with a 38-kHz Teledyne RD

262 Instruments Ocean Surveyor system mounted in the ship's hull (see ship tracks in Fig. S1, Online
263 Supplement). Single ping velocity profiles (60 bins) were sampled, each bin with a vertical length of 16 m
264 (first bin at 30 m) and a maximum sampling depth of 974 m. Additional VM-ADCP data were obtained
265 during cruise 446 of RV Poseidon in February 2013 with a 75-kHz Ocean Surveyor. Here, an 8 m bin length
266 was used and data are available from 24 m downwards.

267 Time-averaged (2 min) ensembles of velocity profiles (RDI Ocean Surveyor raw data format including
268 basic error screening and navigation) were used for data processing with the Common Oceanographic Data
269 Access System (CODAS) (Firing et al. 1995; http://currents.soest.hawaii.edu/docs/adcp_doc/index.html).
270 Processing steps followed the recommendations by Hummon and Firing (2003) and are described in detail
271 by Mohn et al. (2013), including horizontal re-gridding using DIVA (Data Interpolating Variational Analysis;
272 Troupin et al 2012). Error plots are provided in Fig. S1 in the Online Supplement. Additional information on
273 the horizontal advective flow field in the wider region during (October 2009) and just before (September
274 2009) the field study was derived from AVISO altimetry, resolving mesoscale variability.

275 To acquire a better picture of the interaction of barotropic (surface) tides with Senghor seamount,
276 simulations were performed using the non-hydrostatic MITgcm (Marshall et al. 1997) in a two-dimensional
277 (2D) configuration similarly employed by Legg and Huijts (2006) and Legg and Klymak (2008). Simulations
278 were forced by a barotropic N-S flow of the predominant tidal M_2 constituent at a velocity amplitude of
279 5 cm s^{-1} , corresponding to the approximate maximum during spring tides in the region (Egbert and
280 Erofeeva, 2002). The N-S section was chosen as it is expected that the strongest internal tides will
281 propagate in the direction of the major axis of the dominant barotropic M_2 constituent, which is aligned
282 approximately N-S in the region (Siedler and Paul, 1991; Egbert and Erofeeva, 2002; Fig. 1a). The UNESCO
283 equation of state is used and the barotropic flow is forced by a body forcing term in the momentum
284 equation. The simulation was run for 3.5 M_2 tidal cycles.

285 The simulations had realistic initial mass-density stratification with initial temperature and salinity
286 profiles taken from station 812 at N-Ref and smoothed over 20 m vertical bins. Realistic swath-bathymetry
287 was used along the N-S section across the seamount at a longitude of 21.95°W (averaging over 0.05
288 degrees in the longitudinal direction to smooth out some of the local topography). The seamount summit

289 was at the centre of the model domain, with a large region on either side with a uniform depth of 3200 m.
290 The total domain size is 300 km across and 3200 m deep, with a total number of 2000 horizontal grid points
291 and 300 vertical grid points. Horizontal resolution is higher nearer the seamount, where $\Delta x = 55$ m,
292 increasing to $\Delta x = 1$ km away from the topography. In the vertical, resolution is highest in the upper 500 m,
293 where $\Delta z = 2$ m, and Δz increases to 49 m at depth. No-slip boundary conditions are applied at the
294 topography. At the sides, a radiative boundary condition is applied to the baroclinic flow to allow waves to
295 propagate out of the domain.

296 It has to be stressed that the 2D arrangement of these simulations tends to produce unrealistically high
297 absolute current speeds of the baroclinic (internal) tides, unrealistically high rates of kinetic energy
298 dissipation and vertically exaggerated responses, such as displacement of isotherms. Nevertheless, the
299 simulations can be used to demonstrate *where* tides may alter rates of dissipation of turbulent kinetic
300 energy and vertical mixing around the seamount.

301

302

303

304 **3. RESULTS AND DISCUSSION**

305 Before results for ^{234}Th , POC, PN and export can be discussed the physical-oceanographic context
306 needs to be scrutinised to clarify which fluid-dynamic features are of most relevance to this study. This
307 physical-oceanographic context will, therefore, be developed in Section 3.1. The results for ^{234}Th , for POC
308 and PN, and for POC export will then be presented and discussed in Section 3.2, 3.3 and 3.4, respectively.

309

310

311 **3.1 Physical oceanography**

312 **3.1.1 Larger-scale regional flow features**

313 The location of the 36 isohaline at 150 m depth is considered an indicator for the proximity of the CVFZ
314 in the region (Zenk et al., 1991; Martínez-Marrero et al., 2008). In this study we observed the 36 isohaline
315 at between 50 m and 75 m depth at all stations, too shallow to indicate the presence of the CVFZ at

316 Senghor Seamount. Over the long-term, satellite-altimetry-derived average distribution of the surface
317 currents in the wider study region also suggests that the CVFZ rarely reaches Senghor Seamount (Lázaro et
318 al., 2005). Moreover, a time series of remotely sensed regional chlorophyll-*a* distribution in the surface
319 waters shows no evidence of the CVFZ having been anywhere near the seamount or having shed eddies
320 that may have interfered with the processes at the seamount in the ~ 3 months before the cruise and
321 during the cruise (see Fig. S2 in the Online Supplement). The chlorophyll time series also shows that, at the
322 seamount and S-Ref, there were no filaments or eddies shed away from the Mauritanian upwelling during
323 the cruise and during the ~ 3 months before the cruise. However, in October 2009 N-Ref happened to be
324 near the southwestern side of a mesoscale eddy that was associated with high chlorophyll concentrations
325 (Fig. S2). In section 3.1.3 it will be argued that this was close enough to affect the fluid and particle
326 dynamics at N-Ref, questioning its suitability as a reference station for the seamount sites.

327

328 **3.1.2 Interaction of 'background' flow with the seamount**

329 In the study area, background flow consists of the flow components of mesoscale eddies and the quasi-
330 steady 'residual' flow of the basin-scale circulation. A comparison of the AVISO-derived flow field in
331 September 2009 (Fig. 2a) with the flow field in October 2009 (Fig. 2b) reveals that Senghor Seamount was
332 situated amongst mesoscale eddies, with these eddies slowly migrating westwards at a residual background
333 speed of ~ 4 cm s⁻¹. In October, when the vast majority of the samples was collected, there were three
334 mesoscale eddy features: (1) one fairly circular and strongly clockwise-rotating eddy centred around about
335 18.7°N, 20.7°W, i.e., ~ 220 km to the NE of Senghor Seamount; (2) one also fairly circular and strongly
336 clockwise-rotating eddy centred about 16.5°N, 20.0°W, i.e., ~ 220 km to the SE of Senghor Seamount; and
337 (3) an elongated weakly anticlockwise-rotating eddy that reached from about 18.0°N, 24.0°W to about
338 17.0°N, 21.5°W. That is, while sampling was carried out at Senghor, the seamount happened to be located
339 at the ESE end of the elongated weakly anticlockwise-rotating eddy. Comparison of the AVISO-derived
340 regional flow field (Fig. 2b) with the VM-ADCP-derived composite pictures of the flow field at Senghor
341 (Fig. 3) reveals that, just south of the seamount, surface currents were still flowing eastward; just east of
342 the seamount they were turning northward; and to the NE of the seamount they were then turning back

343 and onto the seamount, leading to the surface waters to impinge on the upper seamount from the NE at
344 current speeds of around $\sim 10 \text{ cm s}^{-1}$. This smaller seamount-scale flow vorticity is not resolved by the
345 AVISO map. Maps of remotely-sensed chlorophyll *a* and net primary productivity (NPP) as derived from the
346 Vertically Generalized Productivity Model (VGPM; Behrenfeld and Falkowski, 1997) show that the two
347 clockwise-rotating eddies were sufficiently far from Senghor Seamount so that they had no direct influence
348 on the processes at the seamount (Fig. 2c,d). VM-ADCP data show that the eddies reached no deeper than
349 $\sim 150\text{-}200 \text{ m}$ (Fig. 5,6).

350 During this study NPP was consistently low near and south of the seamount and indicates tropical non-
351 bloom conditions (Maiti et al., 2008). It also appears that S-Ref has been lying in the same type of low-NPP
352 waters that then turned back onto and impinged on the seamount from the NE. By contrast, the wider
353 regional flow field also shows that N-Ref was situated in an area of a strong SW-NE gradient of horizontal
354 current speeds between the anticlockwise eddy and the clockwise northeastern eddy. This means N-Ref is
355 likely to have been affected by horizontal turbulence intensities that were higher than at the other
356 sampling sites of this study. Overall, these circumstances render S-Ref a more suitable reference for the
357 seamount sites than N-Ref.

358 The ADCP data revealed that between $\sim 250 \text{ m}$ and at least $\sim 600 \text{ m}$ (the latter not shown), the
359 background flow was approximately 5 cm s^{-1} to the SSW (Fig. 3), similar to the time-mean flow velocities
360 observed during other studies in this region (Müller and Siedler, 1992; Vangriesheim et al., 2003). There is
361 also interesting evidence for clockwise (looking from above) recirculation around the seamount near the
362 seafloor, with current speeds of comparable magnitude to the background flow between $\sim 400 \text{ m}$ and at
363 least $\sim 600 \text{ m}$ depth (the latter not shown) (Fig. 3). As far as the background flow is concerned, this
364 recirculation constitutes the main distinction between the topmost $\sim 250 \text{ m}$ and the deeper layers of the
365 upper water column above the seamount. This deeper recirculation may have been part of a weak Taylor
366 column (Chapman and Haidvogel, 1992) or due to weak tidal rectification (Goldner and Chapman, 1997).

367 If there was a weak Taylor column, then its vertical extent was limited to waters deeper than $\sim 250 \text{ m}$.
368 This limitation may be due to the strong mass-density stratification in the topmost $\sim 100 \text{ m}$. Composite
369 hydrographic N-S and E-W sections exhibited evidence of isohaline, isotherm and oxygen-isopleth doming

370 towards the summit in the upper ~ 150 m of the water column (see Fig. 9). Doming was also observed by
371 Hanel (2010) in April 2005. The doming of isopleths within the topmost ~ 100 m above and around the
372 summit is, therefore, most likely simply due to somewhat deeper waters being forced up and over the
373 summit plateau while the advected waters pass the seamount rather than due to recirculation around the
374 seamount. Overall, the ADCP and hydrographic results indicate that surface waters (the topmost ~ 200 m)
375 were not trapped at the seamount. Consequently, trapping of nutrients and / or particles at the seamount
376 are very unlikely to have played a significant role for pelagic productivity and particle export from the
377 surface ocean during this study.

378 Finally, it needs to be stressed that there is the possibility that advection of waters past the upper
379 parts of a tall seamount can lead to localised order-of-magnitude enhancement of dissipation of kinetic
380 energy and resulting turbulent mixing (Gibson et al., 1993), with a potential influence on nutrient
381 redistribution and/or particle dynamics at and downstream of the upper seamount. As we have no direct
382 measurements of kinetic energy dissipation, this has to remain a speculative possibility at this point.

383

384 **3.1.3 Interactions of tides with the seamount**

385 In addition to the lower-frequency background flow, other key flow components that could have
386 played a role are higher-frequency tidal and near-inertial ones (Garrett and Kunze, 2007; Alford et al.,
387 2016). VM-ADCP data for the topmost ~ 1000 m indicate that there can be near-inertial oscillations at
388 Senghor Seamount (Fig. 4a). At a latitude of ~ 17°, near-inertial oscillations have a period of ~ 40 hours. The
389 observed oscillations had a predominant E-W component and were more obvious during the first half of
390 the ship time at Senghor. These internal waves phase-propagated downwards, indicating an energy source
391 at depth and probably being a result of the interactions of variable currents with the seamount.

392 In contrast to the near-inertial oscillations tidal oscillations are continuous and therefore probably
393 more important for nutrient redistribution and/or particle dynamics. Near Senghor in the far field, the
394 TPXO barotropic-tide model of Egbert and Erofeeva (2002) predicts the ellipse of the current vector of the
395 predominantly semidiurnal barotropic tide to be strongly elongated in the NNW and SSE direction (Fig. 1a).

396 The NNW-SSE predominance in semidiurnal oscillations is clearly reflected in the VM-ADCP time series
397 obtained at Senghor Seamount in October 2009 (Fig. 4a).

398 The flow components of the barotropic (surface) tide may push water partly over the summit,
399 potentially contributing to isopleth doming and leading to flow acceleration on and near the summit
400 plateau. Furthermore, when mass-density-stratified waters are forced over a topographic obstacle by
401 barotropic tides, internal gravity waves of tidal frequency (internal or baroclinic tides) are generated
402 (Garrett and Kunze, 2007). For topographic obstacles equatorwards of specific critical latitudes, these
403 internal tides can propagate away from their generation sites; by contrast, polewards of the critical
404 latitudes, internal tides are trapped at their generation sites. For diurnal and semidiurnal tides, the critical
405 latitudes are $\sim 30^\circ$ and $\sim 74.5^\circ$, respectively. Senghor is equatorwards of these critical latitudes and it is
406 therefore very safe to assume that trapped internal tidal waves do not occur at Senghor Seamount. Hence,
407 internal tides that are formed at Senghor propagate away from their generation sites. Because of the NNW-
408 SSE predominance of the barotropic tidal forcing it can be assumed that the strongest propagating internal
409 tides occur on the NNW and SSE sides of the seamount, as indicated by the dashed lines in Fig. 3.

410 The MITgcm simulations show that the predominant semidiurnal barotropic tide that interacts with
411 Senghor Seamount leads to the generation of internal-tide beams near the summit of the seamount. In
412 Fig. 4b, the approximate paths of initially upward and downward beams are indicated by thin black and
413 white lines, respectively. The upward beams reflect downwards from the sea surface around 15 km north
414 and south of the centre of the summit plateau. The beam areas are associated with intensified dissipation
415 of kinetic energy, especially in the upper ocean near the seamount (Fig. 4b,c), and with increased maximum
416 current speeds compared to the 'shadow zones' of the water column (Fig. S3).

417 VM-ADCP time series at N-Ref and during transit between N-Ref and the seamount show
418 spatiotemporal current-speed and current-direction changes that are consistent with a beam emanating
419 from Senghor Seamount and reflecting from the sea surface near N-Ref (Fig. 2a,b, S3); this was observed in
420 October 2009 during cruise M79/3 of RV Meteor (Fig. 5a,c,e,g,i) and also in February 2013 during cruise 446
421 of RV Poseidon (Fig. 5b,d,f,h,j).

422 The MITgcm run also predicts that, in addition to beam formation, tidally oscillating flow that is forced
423 over the summit plateau generates soliton-like internal waves that propagate horizontally in the topmost
424 ~ 100 m and north- and southwards away from the seamount. This leads to increased maximum horizontal
425 and vertical flow velocities (Fig. S3) and increased rates of kinetic energy dissipation (Fig. 4) around the
426 summit plateau. Real-world evidence for these waves was also found in the VM-ADCP data: internal waves
427 occurred in the topmost ~ 100 m, have a period of ~ 0.5 hr and appear to propagate predominantly
428 horizontally (they can be seen in Fig. 7, but are more noticeable in the example given in Fig. 8 as the vertical
429 spatial resolution is twice as high and only the topmost 24 m of the ADCP record are blanked out).

430 The VM-ADCP results also revealed that, below the topmost ~ 150-200 m, there can be another type of
431 higher-frequency internal wave that phase-propagates vertically (mostly upwards) and has vertical wave
432 lengths of ~ 100 m and periods that often tend to be shorter than the one of semidiurnal oscillations and
433 certainly shorter than the one of near-inertial oscillations (~ 40 hr). These waves were observed during both
434 October 2009 (Fig. 6,7) and February 2013 (Fig. 8). (They are particularly noticeable in the current
435 directions between day 288.7 and 290.7 in Fig. 6e and 7e, also in current speed up to day 290.7 in Fig. 7d,
436 and in u , v , current speed and current direction in Fig. 8). The fact that these waves were observed in
437 October 2009 *and* in February 2013 is relevant as Senghor Seamount was located differently relative to
438 nearby mesoscale eddies: in October 2009, Senghor was in the easternmost part of an elongated weak
439 anticlockwise eddy (Fig. 2b), whereas in February 2013, Senghor was in the NW quarter of a strong circular
440 westward-moving anticlockwise eddy (not shown). Therefore, the location of Senghor Seamount relative to
441 the mesoscale eddies seems to be unlikely to play an important role for these vertically phase-propagating
442 higher-frequency internal waves.

443 The prevailing upward phase propagation indicates downward energy propagation and an energy
444 source higher up in the water column. These waves became particularly prominent near / during spring
445 tides when peak semidiurnal barotropic current speeds were $\geq 4.5 \text{ cm s}^{-1}$ (see Fig. 6e: after day 288.7, when
446 peak barotropic speeds start exceeding 4.5 cm s^{-1} (Fig. 6a), the waves become more obvious and can be
447 seen up to day 290.7 in Fig. 7; the waves are also a constant feature in February 2013 when barotropic tidal
448 current speeds were continuously $> 4.5 \text{ cm s}^{-1}$). The findings that the waves were most prominent in waters

449 above the seamount slopes (Fig. 6-8), may reach northwards to at least the waters above the seamount rise
450 (Fig. 7), did not occur at N-Ref (Fig. 5) and only occurred very faintly at S-Ref (Fig. 7), further support the
451 notion that the waves were generated at Senghor Seamount.

452 Overall, the evidence suggests that these higher-frequency internal waves were tidally generated at
453 the seamount. Given the short wave periods and short vertical wave lengths, these waves might be (related
454 to) higher harmonics of the internal-tide beams that emanate from the uppermost parts of Senghor
455 Seamount (this is especially likely to be the case for largely supercritical seamounts such as Senghor
456 Seamount; Lamb, 2004). Because of the short wave lengths these waves may dissipate relatively quickly,
457 contributing to increased rates of energy dissipation near the upper seamount, especially when they
458 interact with the high mass-density stratification in the pycnocline.

459 Finally, there is also hydrographic evidence for the importance of tidally generated higher-frequency
460 internal waves at this seamount. Instantaneous mixed-layer thicknesses ranged from only ~ 5 m up to
461 ~ 20 m (Fig. 10,11). Underneath the mixed layer was an abrupt pycnocline where the main part of the
462 pycnocline was only ~ 5-20 m thick. At stations where several mass-density profiles could be obtained (e.g.,
463 N-Ref: Fig. S4) mixed-layer and pycnocline thicknesses varied temporally on time scales as short as hours to
464 days. And at greater depths of 100s of meters, there were fairly abrupt vertical shifts (by 10s of meters) of
465 isohalines, isotherms and oxygen isopleths across the seamount (Fig. 9). Due to the paucity of the
466 hydrographic dataset it is impossible to tell whether this is temporal or spatial variability or both. In any
467 case, the existence of these abrupt shifts and the evidence for temporally highly variable mixed-layer and
468 pycnocline thicknesses suggest that fluid dynamics around the upper seamount can be vigorous, probably
469 due to the higher-frequency seamount-generated internal waves.

470 In summary, there are several lines of evidence indicating that tides play a prominent role in
471 controlling fluid dynamics at Senghor Seamount. This could have implications for nutrient redistribution
472 and particle dynamics in the topmost few 100s of meters of the water column around the seamount,
473 potentially influencing POC export.

474

475

476 3.1.4 Physical oceanography: summary and conclusion

477 The available physical-oceanographic information leads to the following conclusions regarding the flow
478 dynamics around Senghor Seamount at the time of the study (Objective O1). (1) Larger-scale regional
479 features such as the CVFZ and the Mauritanian upwelling system did not play a role for this study. (2) S-Ref
480 can be used as a reference site for the seamount stations. (3) Within the topmost ~ 200 m of the water
481 column, low-frequency background flow impinged on the seamount from the northeast, contributing to
482 isopycnal doming over the summit. (4) At depths greater than ~ 200 m and down to at least ~ 600 m, there
483 is evidence for clockwise recirculation of near-seafloor waters around the seamount (a deep Taylor column
484 and / or weak tidal rectification); there is no evidence for seamount-trapping of near-seafloor waters in the
485 topmost ~ 200 – 250 m. (5) Higher-frequency fluid dynamics were primarily influenced by barotropic tidal
486 forcing, leading to the generation of internal-tide beams and soliton-like internal waves that preferentially
487 propagate away to the north and south and are thought to form a N-S 'screen' of intensified kinetic energy
488 dissipation (and probably intensified vertical mixing) that runs across the upper seamount. (6) In the
489 topmost hundreds of meters of the water column, another type of internal wave was observed over the
490 seamount slopes and also further towards the north and south away from the seamount. These waves are
491 also likely to be seamount-generated, could be higher harmonics of the main internal tide, and probably
492 also contribute to the screen of increased rates of energy dissipation that runs across the upper seamount.
493 (7) As the dissipation screen was orientated approximately orthogonally to the low-frequency background
494 inflow from the NE, the waters of the background flow were passing through this screen at the time of this
495 study.

496 The main physical-oceanographic result is that tides seem to play a key role in controlling the fluid
497 dynamics at Senghor Seamount and result in a screen of enhanced kinetic energy dissipation that runs
498 across the seamount in the NNW-SSE direction and was traversed by the background flow at the time of
499 this study. The distribution of dissipation of kinetic energy is likely to be of importance for seamount
500 biogeochemistry as it may influence vertical mixing (Waterhouse et al., 2014) (and therefore nutrient
501 redistribution) and potentially also particle aggregation and / or disaggregation (and therefore vertical flux
502 of particulate matter) (Burd and Jackson, 2009).

503

504

505 **3.2 Thorium-234**

506 **3.2.1 Distribution of total and particulate ²³⁴Th**

507 Total ²³⁴Th activities (A_{Th}^t) in the topmost 250 m of the water column ranged from 1.46 up to
508 2.62 dpm L⁻¹ (Tab. 2). At all sites there were significant ²³⁴Th/²³⁸U disequilibria ($A_{Th}^t < A_U$), almost always
509 located within the topmost 75 m, i.e., reaching well below the surface mixed layer (Fig. 10,11). There was
510 no evidence for ²³⁴Th excess ($A_{Th}^t > A_U$) which is sometimes observed right below the surface layer and
511 interpreted in terms of rapid particulate-matter breakdown.

512 Particulate ²³⁴Th activities (A_{Th}^p) of the > 53 μm samples (Tab. 3) were always higher at 50 m depth (32 m
513 depth at N-Ref) compared to 150 m depth (90 m at the Summit). The highest value at 50 m was found
514 above the summit plateau (0.071 ± 0.018 dpm L⁻¹) and the second highest at N-Slope
515 (0.036 ± 0.002 dpm L⁻¹); the lowest occurred at S-Ref (0.015 ± 0.000 dpm L⁻¹). The highest value at 150 m
516 depth was found at N-Slope (0.032 ± 0.005 dpm L⁻¹) and the lowest at W-Slope (0.009 ± 0.000 dpm L⁻¹). The
517 general range of values is very similar to the range of values found by Owens et al. (2015) in this study area
518 at the end of October 2010.

519 Activities of the 0.7 – 53 μm samples in the topmost 150 m (Tab. 3) were found to be
520 0.044 ± 0.016 dpm L⁻¹ up to 0.227 ± 0.023 dpm L⁻¹ (average: 0.144 dpm L⁻¹). The higher activity values of this
521 study are very similar to values reported by Owens et al. (2015) for the surface waters of the same region in
522 late October 2010. The values from the Summit, however, look low (about 1/2 to 1/4) in comparison to the
523 results of Owens et al. (2015). Unfortunately, our ²³⁴Th data set for 0.7 – 53 μm particles is incomplete as
524 not all relevant depths and locations could be sampled.

525

526 **3.2.2 Thorium-234 export fluxes**

527 As outlined by Owens et al. (2015), in previous studies different approaches have been used to define
528 the water layer for which export fluxes are calculated (the 'export layer'). There seem to be three main
529 procedures: (1) The export layer is defined through the depth at which ²³⁴Th / ²³⁸U equilibrium is reached.

530 This approach typically takes into account the combined effect of both near-surface disequilibria where A_{Th}^t
 531 $< A_U$ and excess layers where $A_{Th}^t > A_U$ (if present). (2) In some cases disequilibria reach into waters that are
 532 deeper than the photosynthetically active surface waters. The export layer is then defined based on the
 533 layer of water in which active photosynthesis is thought to take place. This approach in itself has taken
 534 different forms and was based on, for instance, the 1%-depth-level of photosynthetically active radiation
 535 (PAR), the 10%-depth-level of maximum chlorophyll fluorescence, or estimates of the 'compensation
 536 depth' where gross photosynthetic organic-carbon production and organic-carbon respiration cancel each
 537 other out and NPP is zero. (3) In some cases a comparatively arbitrary depth was chosen as the lower
 538 boundary of the export layer. A number of studies have used the 100 m cut-off.

539 Owens et al. (2015) showed for our study region that water layers with disequilibria $A_{Th}^t < A_U$ coincided
 540 very well with the distribution of photosynthetically active organisms. We, therefore, chose the first of the
 541 above approaches (the equilibrium-depth approach) to calculate ^{234}Th export for this study. However, to
 542 facilitate direct comparison with studies that used the '100 m-cut-off' approach, additional export-flux
 543 calculations were carried out using 100 m as the lower boundary of the export layer.

544 In order to estimate the net ^{234}Th -flux (P) from the disequilibrium layer, a single-box steady-state model
 545 (Coale and Bruland, 1987; Savoye et al., 2006) was applied according to

$$546 \quad P = \lambda \int_0^z (A_U - A_{Th}^t) dz \quad (1)$$

548 where λ is the decay constant of ^{234}Th ($\lambda = \ln 2 / t_{1/2} \approx 0.02876 \text{ d}^{-1}$) and z is the depth at which $^{234}Th / ^{238}U$
 549 equilibrium is met. An implicit assumption of Eq. 1 is that there is no net physical-oceanographic transport
 550 of ^{234}Th into or out of a sampling site due to turbulent diffusion and / or advection that is superimposed on
 551 spatial A_{Th}^t gradients.

553 At most stations equilibrium was reached at 75 m; only at N-Ref it was reached already at 60 m. Because
 554 of the shallow water above the summit plateau and the possible influence of resuspension on ^{234}Th
 555 dynamics in the water column it is not possible to unequivocally identify the export layer for the Summit
 556 station. However, an equilibrium value was detected at 75 m depth at the Summit site and $z = 75 \text{ m}$ was

557 therefore used to estimate a notional export value for this location. The robustness of this estimate will be
558 discussed in more detail in Section 3.4.2 below.

559 ^{234}Th export fluxes that were derived through the equilibrium-depth approach ranged from 616 ± 61
560 up to $1306 \pm 90 \text{ dpm m}^{-2}\text{d}^{-1}$, with errors given as 1 propagated standard deviation (1SD) (Fig. 12a; Tab. 4). In
561 the far field, a greater flux was found for N-Ref compared to S-Ref. Significant differences were observed
562 between some of the seamount sites: most notably, the W-Slope site displayed the highest flux of all the
563 slope sites ($1306 \pm 90 \text{ dpm m}^{-2}\text{d}^{-1}$) at approximately twice the estimated magnitude of flux observed at the
564 S-Slope ($712 \pm 104 \text{ dpm m}^{-2}\text{d}^{-1}$) and even being slightly higher than at N-Ref ($990 \pm 61 \text{ dpm m}^{-2}\text{d}^{-1}$). Flux
565 estimates that were derived by the '100 m-cut-off' approach were indistinguishable from, or only slightly
566 higher than, the results of the equilibrium-depth approach (Fig. 12a; Tab. 4).

567 Before the ^{234}Th flux results can be used to calculate POC export, two key assumptions of Eq. 1 need to
568 be scrutinised: the steady-state assumption and the assumption of negligible net physical-oceanographic
569 transport of ^{234}Th . This is done in detail in the Online Supplement S5. In summary, the seamount sites N-
570 Slope, S-Slope, Summit and W-Slope are likely to be associated with underestimates of ^{234}Th export fluxes.
571 The highest underestimate probably occurred for W-Slope as there is a combination of the effects of net
572 advective input and sustained vertical mixing. The extent of the underestimate at Summit is uncertain
573 because of the possible added influence of resuspended sediments on ^{234}Th dynamics (see the more
574 detailed discussion in Section 3.4.2). Overall, however, it seems safe to conclude that all seamount sites
575 have higher ^{234}Th export fluxes than S-Ref; and there is strong evidence for increasing export in the
576 downstream direction across the seamount. For completeness, it also needs to be stressed that, because of
577 the low zooplankton (< 20 mm) biomass at Senghor Seamount (< $0.1\text{-}0.2 \text{ g m}^{-3}$ in the topmost ~ 100 m of
578 the water column: Denda and Christiansen, 2014; Denda et al., 2016), zooplankton-associated vertical
579 transport of ^{234}Th is most certainly negligible in this area (Rodriguez y Baena et al., 2006).

580

581

582 **3.3 Particulate organic carbon (POC) and particulate nitrogen (PN)**

583 In the > 53 μm size fraction, POC and PN concentrations were often higher at 50 m (32 m at N-Ref) than
584 at 150 m (90 m at the Summit) (Tab. 5). Particles > 53 μm are thought to constitute the bulk of the settling
585 flux into the deep interior ocean and the decreasing concentrations with increasing depth support the view
586 of active export of particulate matter. In the far field there is an approximate halving of POC and PN
587 concentrations in the > 53 μm size fraction if one compares N-Ref to S-Ref. The seamount is also associated
588 with significant variability. At 50 m POC concentrations at the seamount were $\sim 2 - 5$ times higher than at S-
589 Ref, suggesting a seamount effect on the formation of larger particles. POC concentrations at the seamount
590 at 150 m were up to ~ 4 times higher than at S-Ref, also suggesting a seamount effect; however, the effect
591 is reduced compared to 50 m. Interestingly, the POC concentration at W-Slope at 150 m is very low and
592 similar to the low POC concentration at S-Ref at 150 m. This low POC concentration at 150 m in
593 combination with a still comparatively high POC concentration at 50 m and a high ^{234}Th export flux estimate
594 suggests that the waters sampled at W-Slope were strongly affected by recent or ongoing export of
595 particulate matter. This view is also supported by the higher concentrations at 50 m and especially 150 m at
596 the N-Slope station that is located upstream of W-Slope: as W-Slope is the downstream seamount station
597 the results from this station can be interpreted in terms of a maturing seamount-derived export signal.

598 Broadly speaking, the horizontal concentration trends at 50 m are qualitatively similar for the 0.7-53 μm
599 size fraction, but absolute concentrations were much higher (by about an order of magnitude) than in the
600 > 53 μm size fraction (Tab. 5). At 150 m POC concentrations in the 0.7-53 μm size fraction were generally
601 low across the study region. However, at the seamount, significant POC concentration drops (by factors of
602 $\sim 2 - 7$) occurred in the 0.7-53 μm size fraction if one moved from 50 m to 150 m; by contrast, the
603 concentrations at 50 m and 150 m at S-Ref were very similar and low. This suggests formation of particulate
604 material in the topmost 10s of meters of the water column at the seamount. Finally, at 50 m, the molar C/N
605 ratios ($\sim 10 - 11$) for the organic matter in the 0.7-53 μm size fraction are higher more upstream (N-Slope
606 and S-Ref) than at the other more downstream seamount stations ($\sim 6 - 8$), possibly indicating that the
607 formed particles contain comparatively fresh (N-rich) organic material. Overall, the POC- and PN-derived
608 information points to formation of fresh particulate organic matter in the near-surface waters at the
609 seamount.

610

611

612

613 3.4 POC export flux

614 Estimates of POC export fluxes can now be derived by multiplying the ^{234}Th -export flux, P (Eq. 1), with
615 the $\text{POC} / A^{\text{P}}_{\text{Th}}$ ratio on the larger faster-settling particles ($> 53 \mu\text{m}$). For the topmost few 100s of meters of
616 the oceanic water column, it has been shown that the $\text{POC} / A^{\text{P}}_{\text{Th}}$ ratio on settling particles often decreases
617 with depth, with much of the overall decline completed within the topmost 100 m of the water column and
618 the steepest part of the drop occurring in the topmost tens of meters (Buesseler et al., 2006; Owens et al.,
619 2015). The choice of depth from which to derive $\text{POC} / A^{\text{P}}_{\text{Th}}$ ratios may, therefore, significantly influence the
620 outcome of the POC export flux calculation and its uncertainty.

621 In this study we are interested in POC export *from* the export layer into the deep interior water column
622 and not in vertical flux distribution *throughout* the export layer or export that only reaches the twilight
623 zone. To arrive at such export estimates for all sites (except Summit which is too shallow), the $\text{POC} / A^{\text{P}}_{\text{Th}}$
624 ratios determined for particles $> 53 \mu\text{m}$ at 150 m were used. Despite the high level of confidence in this
625 original approach (ED/150: ^{234}Th flux at equilibrium depth (ED) and $\text{POC}/A^{\text{P}}_{\text{Th}}$ ratio at 150 m depth), three
626 additional approaches were applied to calculate estimates of POC export. This was done to facilitate
627 comparison with other studies that used the '100 m cut-off' approach for ^{234}Th export calculations and to
628 consider further potential sources of uncertainty. The first additional approach (100/150) used $\text{POC} / A^{\text{P}}_{\text{Th}}$
629 values from 150 m and ^{234}Th fluxes calculated based on integrated disequilibria down to 100 m. The second
630 additional approach (ED/ED) used $\text{POC} / A^{\text{P}}_{\text{Th}}$ values for the equilibrium depth, based on linear interpolation
631 of the values found at 50 m and 150 m, and ^{234}Th fluxes calculated based on the equilibrium depth. The
632 third additional approach (100/100) used $\text{POC} / A^{\text{P}}_{\text{Th}}$ values for 100 m, based on linear interpolation of the
633 values found at 50 and 150 m, and ^{234}Th fluxes calculated based on integrated disequilibria down to 100 m.
634 The results of all these calculations are compiled in Fig. 12b and Tab. 4. Uncertainties were propagated
635 from the ^{234}Th export estimates and $\text{POC} / A^{\text{P}}_{\text{Th}}$ ratios and given as $\pm 1\text{SD}$ and with the relative 1SD
636 uncertainties ranging from 15% up to 37% of the mean. All four approaches result in similar values (Fig.

637 12b), providing confidence in the export estimates and allowing for a comparison of the different sampling
638 stations. In the following, the distribution of POC export fluxes will be described (Objective O2).

639

640 **3.4.1 Far Field**

641 Similar to the POC and PN concentration data, the POC-flux estimates displayed a N-vs.-S difference in
642 the far field, with values at N-Ref being more than three times higher than at S-Ref. The monthly maps of
643 NPP as derived from the VGPM for September and October 2009 suggest there was NPP variability in the
644 far field on the mesoscale (10-200 km) and possibly also on the sub-mesoscale (1-10 km) (Fig. 2c,d).
645 However, the NPP values were generally low and several studies in other subtropical and tropical ocean
646 regions (near Hawaii: Maiti et al. (2008); at Station ALOHA: Benitez-Nelson et al. (2001b), Karl et al. (1996);
647 at BATS: Michaels and Knap (1996)) have shown that there tends to be a lack of a clear relation between
648 primary productivity levels and export of particulate carbon. This notion is supported by the fact that in the
649 Senghor region NPP varied by a few 10s of percent at most while POC export at the two far-field sites
650 differed by a factor of > 3. Hence, the difference between export at N-Ref and S-Ref more likely reflects a
651 difference in factors other than NPP that control export. As mentioned above, in October 2009, a major
652 physical-oceanographic difference between N-Ref and S-Ref was the mesoscale horizontal current-speed
653 gradient: at N-Ref it was high in the SW-NE direction and very weak at S-Ref and at the seamount (Fig. 2b).
654 Higher horizontal velocity gradients increase shear and therefore also horizontal turbulence and energy
655 dissipation. Such increased energy dissipation can lead to shear-driven aggregation of smaller, slower-
656 settling into larger, faster-settling particles and, hence, increased export. This view is consistent with the
657 increased ²³⁴Th export fluxes that Maiti et al. (2008) found at the rim (rather than the centre) of an intense
658 cyclonic (anticlockwise-rotating) eddy downstream of Hawaii. This aggregation mechanism is likely to have
659 led to increased export at N-Ref, without a significant rise in NPP. At S-Ref this mechanism is weaker and
660 NPP is also low, explaining the low observed export.

661 Another fluid-dynamic difference between N-Ref and S-Ref is the fact that N-Ref is located within the
662 area where the initially downward semidiurnal internal-tide beam that emanates from the uppermost
663 northern slope of the seamount reflects from the sea-surface for the first time, whereas S-Ref lies outside

664 the respective surface-ocean area on the southern side of the seamount (Fig. 2a,b, 5, S3). The sea-surface
665 reflection areas are likely to be associated with enhanced energy dissipation that could translate into
666 increased shear-driven aggregation and export. This is also further evidence to support the notion that S-
667 Ref is better suited as a reference for the seamount sites than N-Ref.

668 Finally, we include a note of caution that relates to the possible effect of atmospheric dust input. In
669 the Introduction it was mentioned that large amounts of dust particles that are incorporated into marine-
670 snow aggregates could lead to increased mass densities of these aggregates and, hence, higher settling
671 speeds and POC export (e.g., Fischer et al., 2016). In the week prior to the start of the sampling for this
672 study, a comparatively dense remotely-(MODIS-)sensed plume of dust was swept from Africa offshore and
673 across the study region (not shown). At its most intense (probably 21-23 Sept 2009) the plume covered the
674 whole study region and looked horizontally homogeneous. Only after this peak phase the atmospheric dust
675 distribution was more heterogeneous in the form of dust filaments that were discernible until the end of
676 Sept 2009. In contrast to the initial main plume with a latitudinal width of more than 1000 km, the
677 subsequent filaments with widths of typically ~ 100 - 200 km might have caused spatial patchiness of dust
678 input to the surface ocean. That is, it is highly unlikely that on the large scale of the main plume and the
679 short scales of the distances between seamount sites patchy dust input played a role; however, the dust
680 filaments could have introduced differences in dust input on scales similar to the distance between N-Ref
681 and S-Ref. It can be concluded that, when comparing export amongst the seamount sites and between the
682 seamount sites and S-Ref, patchy dust input is unlikely to have played a significant role.

683

684 **3.4.2 POC export fluxes at the seamount**

685 Based on the above considerations regarding the reference sites, it can now be concluded that the
686 seamount leads to a general increase of POC export (Objective O3): on the upstream side (E-Slope) and on
687 the sides of the seamount, looking downstream (S-Slope, N-Slope), POC export is about twice as high as at
688 S-Ref; on the Summit and on the downstream side (W-Slope), POC export is even ~ 3 - 4 times higher than
689 at S-Ref (Fig. 12b). In Section 3.2.2 it was argued that ^{234}Th export fluxes for N-Slope, W-Slope, S-Slope and
690 Summit are underestimates. Such underestimates of ^{234}Th export would translate into underestimates of

691 POC export. That is, true POC export estimates for these sites might have been even higher and deviate
692 even more strongly from export at the upstream E-Slope site and S-Ref in the far field. Because of the
693 shallow waters at Summit and the different positions of the other seamount sites relative to the impinging
694 background flow and impinging barotropic tides, the slope sites and Summit will now be discussed
695 separately, with the aim of proposing likely mechanistic scenarios that can explain their special features.

696

697 **3.4.2.1 POC export fluxes at the slope sites**

698 As mentioned above, when the far-field surface waters impinge on the seamount from the NE and pass
699 the seamount, they are thought to pass through a tidally generated NNW-SSE screen of intensified energy
700 dissipation and small-scale mixing. This could have two sudden effects: (1) an increased upward flux of
701 nutrients into the euphotic zone that leads to a short pulse of primary production of new particulate
702 matter; and (2) enhanced shear-driven aggregation of smaller, slower-settling into larger, faster-settling
703 particles. Both effects could lead to increased export.

704 That such sudden nutrient input can in fact translate into brief export 'spikes' was shown by Buesseler et
705 al. (1992) during the North Atlantic Bloom Experiment (NABE). Within about one day, storm-related vertical
706 mixing led to a clearly detectable increase of nitrate concentration in the topmost water layers (see their
707 Fig. 1). They also demonstrated that this abrupt increase was followed by an equally rapid reduction in the
708 nitrate concentration and a concomitant drop in total ²³⁴Th concentrations, suggesting that the sudden
709 nutrient supply was rapidly converted into a moderate export flux of particulate matter.

710 In analogy, at Senghor, surface waters passing through the screen of enhanced mixing could have been
711 associated with a similarly sudden and moderate increase in primary productivity and particle export.
712 Moreover, after the waters have passed through the tidally generated mixing in the NNW-SSE screen,
713 elevated mixing intensities (and nutrient supply into the euphotic zone) could still be sustained for several
714 kilometres downstream of the 'screen' due to increased rates of energy dissipation in waters that were
715 advected past the seamount (Gibson et al., 1993). In the NW quarter of the seamount, N-Slope is likely to
716 be situated within the dissipation screen whereas W-Slope was most likely located downstream (to the SW)

717 of the screen and of N-Slope. Export fluxes at W-Slope can therefore be expected to be higher than export
718 fluxes at N-Slope; and this is what was found.

719 There is a biogeochemical indicator that supports the proposed scenario involving increased
720 productivity. Production of molecular oxygen (O_2) through photosynthesis can lead to shallow subsurface
721 maxima of the concentration of dissolved oxygen (DO) in the euphotic zone (Hayward, 1994). Such maxima
722 were observed in DO profiles between ~ 10 m and ~ 50 m at almost all CTD stations across the study area
723 (examples can be seen in Fig. 10,11). Depth-integration of the amount of DO in this subsurface peak above
724 the 'background' concentration in the surface mixed layer yields an estimate of the 'excess' DO inventory in
725 this water layer which can be interpreted as an approximate measure of photosynthetic activity.

726 Excess DO inventories together with the integration depths and maximum DO concentrations for each
727 profile are given in Tab. 6. The highest excess DO inventories were found at station 891 (seafloor at 705 m
728 water depth) that lies near the streamline that connects N-Slope and W-Slope, and at station 920 (2805 m
729 water depth at the seafloor) that also lies on the NW-Slope but further away from the streamline that
730 connects N-Slope and W-Slope (Fig. 1b,3). At sites where repeat CTD casts were performed some temporal
731 variability in DO inventories was displayed which may be due to the aforementioned passing internal
732 waves. However, even if this variability is taken into account, the DO inventories on the NW slope stand out
733 (Tab. 6). The high DO inventories above the NW slope, therefore, support the notion of pulsed productivity
734 in waters passing from the northern to the western slope areas.

735 Unfortunately, there is no downstream station for S-Slope to scrutinise whether a signal comparable to
736 the one of W-Slope formed above the SW side of the seamount. However, the remotely sensed NPP
737 distribution at the time of this study showed a 'banner cloud' of slightly elevated NPP values to the SW
738 (downstream) of the seamount (Fig. 2d) which may have resulted from a moderate seamount-driven
739 increase of primary productivity downstream of N-Slope as well as S-Slope. This view is supported by the
740 fact that in September 2009 there was also evidence for such a 'banner cloud' of slightly enhanced NPP on
741 the downstream side of the seamount (then, on the eastern side: Fig. 2c).

742 As mentioned above, it is known that increased rates of energy dissipation can lead to enhanced shear-
743 controlled aggregation of smaller, more slowly settling particles into larger, more rapidly settling particles

744 (Burd and Jackson, 2009). For open-ocean waters, the upper validity threshold of this positive relationship
745 is still not well defined, but the limited available information suggests it may be near $10^{-7} - 10^{-6} \text{ m}^2\text{s}^{-3}$, with
746 net disaggregation prevailing at higher rates of energy dissipation (Alldredge et al., 1990; Berhane et al.,
747 1997). In internal-tide beams and downstream waters of tall seamounts, rates of energy dissipation can
748 reach up to $10^{-7} - 10^{-6} \text{ m}^2\text{s}^{-3}$ (Lueck and Mudge, 1997; Johnston et al., 2011) (for comparison, the global
749 average at 150 m depth is $2 \times 10^{-8} \text{ m}^2\text{s}^{-3}$ (Whalen et al., 2012); and for an average trade-wind speed of
750 5.5 m s^{-1} the surface-ocean relation between wind speed and dissipation reported by MacKenzie and
751 Leggett (1993) finds $10^{-8} \text{ m}^2\text{s}^{-3}$ for a depth of 50 m). If dissipation rates are the same in the screen at
752 Senghor Seamount, then, particles that pass the screen and travel in downstream waters are expected to
753 be exposed to increased rates of energy dissipation that foster aggregation into larger faster-settling
754 particles, contributing to the increased export fluxes. Evidence for this process was found in that, at 150 m
755 depth at W-Slope, the second-lowest POC and PN concentrations were observed in the $> 53 \mu\text{m}$ size
756 fraction (only S-Ref displayed a slightly lower absolute POC concentration and a similar PN concentration).
757 These low concentrations may well be the result of enhanced particle export due to the shear-driven net
758 aggregation of smaller, slower-settling into larger, faster-settling particles.

759

760 **3.4.2.2 POC export flux at the Summit**

761 For the Summit, three factors need to be considered when judging the calculated POC export.

762 (1) Because of the shallow waters on the Summit the export estimates for this station may have been
763 affected by resuspended sediments as resuspension of sediments would lead to intensified scavenging of
764 ^{234}Th (e.g., Turnewitsch et al., 2008). As discussed in Section 3.2.2, resuspension may have only affected the
765 first $\sim 10\text{-}20 \text{ m}$ above the seafloor which means that the estimated ^{234}Th export flux would not have been
766 strongly biased by resuspension. (2) However, moderate resuspension may have influenced the
767 composition of particles in the $> 53 \mu\text{m}$ particle size fraction at 90 m that were used to calculate the POC
768 export flux. The POC / ^{234}Th ratio of $7.1 \mu\text{mol dpm}^{-1}$ for $> 53 \mu\text{m}$ particles from 90 m depth was the highest
769 measured value in the near-surface waters of the study area. That is, using the POC / ^{234}Th ratio from 90 m

770 depth may have led to an *overestimation of the POC export flux*. The lower export estimate that was based
771 on the POC / ^{234}Th ratio at the equilibrium depth (75 m), with the value being derived by linear
772 interpolation between the values from 50 m and 90 m, is probably less biased by resuspension. (3) Finally,
773 non-negligible upward net transport of ^{234}Th into the export layer by enhanced tidally driven vertical mixing
774 and upwelling (doming) around the summit area may have led to an *underestimation* of values for both
775 ^{234}Th and POC export. Although the net effect of the second and third factor is unknown, it seems safe to
776 conclude that export at the Summit is high in comparison to E-, N- and S-Slope.

777 This conclusion is supported by the highest POC concentration in the $> 53 \mu\text{m}$ particle size at 50 m
778 depth, combined with POC concentrations in the $0.7\text{-}53 \mu\text{m}$ particle size fraction at 50 m that are low
779 ($16.5 \mu\text{g L}^{-1}$) in comparison to the respective concentrations at stations that are more upstream (N-Slope:
780 $30.2 \mu\text{g L}^{-1}$; E-Slope: $21.0 \mu\text{g L}^{-1}$), indicating conversion of smaller, more slowly settling particles into larger,
781 more rapidly settling ones. That is, aggregation had started and resulted in enhanced export; but the
782 process hadn't matured as much as it had done at the more downstream W-Slope where much of the
783 $> 53 \mu\text{m}$ particles had been exported already. A moderate and sudden increase in the export of locally
784 primary-produced particles may also have contributed to this overall enhancement of POC export over the
785 Summit, as reflected by excess DO inventories that are higher in comparison to the upstream E-Slope site
786 (Tab. 6).

787

788

789

790 **4. SUMMARY AND CONCLUSIONS**

791 This study aimed to look for an influence of flow / topography interactions at a ~ 3200 m-tall seamount
792 that reaches up to ~ 100 m beneath the sea surface on export of POC from the surface (the topmost
793 ≤ 100 m) into the deeper ocean. The main part of the study was carried out when both primary productivity
794 and mesoscale productivity patchiness were low in the wider study region. The background flow was
795 impinging on the seamount from the NE. There was no seamount-trapping of waters in the topmost
796 ~ 200 m. Tidally generated internal waves are formed mainly on the upper northern and southern slopes of

797 the seamount, probably resulting in a 'screen' of high rates of energy dissipation that runs across the
798 seamount in the NNW-SSE direction. Hence, the background currents traversed the screen while flowing
799 past the seamount.

800 The comparison between the southern reference site and seamount sites revealed what is interpreted
801 as a detectable seamount effect on POC export: calculated POC export at the seamount sites was
802 ~2-4 times higher than at the southern reference site. Therefore, the core hypothesis of this study that a
803 tall seamount can trigger enhanced localised POC export is accepted. It can also be concluded that the POC
804 export fluxes increase while the passing waters are advected from the NE towards the SW around and over
805 the seamount, with the highest fluxes occurring on the downstream side of the seamount. This supports
806 the view that biogeochemical and biological effects of tall seamounts in surface-ocean waters might be
807 strongest at some (downstream) distance from, rather than centred right above, the seamount summit
808 (e.g, Genin et al., 2004).

809 The tidally generated screen of high rates of energy dissipation that runs across the seamount is
810 proposed to result in a combination of two main factors that led to the increased POC export above the
811 seamount: (1) increased upward transport of nutrients into the euphotic zone, driving sudden, brief pulses
812 of primary production of new particulate matter, followed by the particles' export into deeper waters; and
813 (2) pulses of increased shear-driven aggregation of smaller, slower-settling into larger, faster-settling
814 particles.

815 It can be speculated that a variant of the shear-based mechanism may also affect deeper seamounts
816 and possibly even abyssal hills by controlling aggregate sinking speeds in the vicinity of the hill or seamount
817 feature. This could relate to deposition rates and patterns of particulate matter on and near the feature
818 (Durden et al., 2015; Turnewitsch et al., 2015; Morris et al., 2016) and could have implications for the
819 concept of topographic 'stepping stones' for dispersion and migration of deep ocean fauna as well as for
820 general drivers of spatial environmental heterogeneity in the deep sea.

821 Given the environmental variability in the study region, it is likely that distribution and magnitude of
822 seamount-controlled POC export vary in space and time. Factors that contribute to this variability and
823 might at times even overwhelm the seamount effects include seasonal variability of productivity (Lutz et al.,

824 2007; Arístegui et al., 2009; Kiriakoulakis et al., 2009; Vilas et al., 2009), different types (clockwise,
825 anticlockwise) of mesoscale eddies (Onken and Klein, 1991; Bashmachnikov et al., 2009), variable mineral
826 dust inputs from the Sahara (Chiapello and Bergametti, 1995; Ratmeyer et al., 1999a,b; Brust and Waniek,
827 2010; Fitzsimmons et al., 2013), and high-productivity filaments and eddies extending from the Mauritania
828 Upwelling into the Senghor Seamount area (Bory et al., 2001; Hagen, 2001; Meunier et al., 2012). What also
829 remains unclear is how strong the biogeochemical influence of remotely generated internal tides can
830 become when they propagate through the study area.

831 Keeping these caveats in mind, this study shows that, under certain conditions, there can be an effect
832 of a tall seamount on local and possibly regional surface-ocean biogeochemistry, with tidal dynamics
833 playing a prominent role. It can be speculated that these effects control the spatiotemporal distribution of
834 magnitude and nutritional quality of the flux of food particles to the benthic and benthic-pelagic
835 communities at and near the seamount. This variability may then translate into variable pelagic and benthic
836 community distributions around the different slopes of the topography. If there is 'bottom-up' forcing on
837 seamount biogeochemistry and biology (Rowden et al., 2010), then the nature of that forcing is also likely
838 to vary between different seamounts, depending on where the seamount is situated within the fluid-
839 dynamic parameter space that describes flow / topography interactions at seamounts (Turnewitsch et al.,
840 2013).

841

842

843

844 **Acknowledgements**

845 We thank four anonymous reviewers for constructive comments that helped improve the manuscript.
846 Samples and field data for this study were obtained during cruise M79/3 of RV Meteor and cruise 446 of RV
847 Poseidon, and we thank the officers and crew for their contributions to this work. This study was supported
848 through grant NE/G006415/1 of the UK's Natural Environment Research Council (NERC) and grant 669947
849 of the European Research Council (ERC).

850

851 **REFERENCES**

852 Alford, M.H., MacKinnon, J.A., Simmons, H.L., Nash, J.D., 2016. Near-inertial internal gravity waves in the
853 ocean. *Annual Review of Marine Science* 8, 95-123.

854 Alldredge, A.L., Granata, T.C., Gotschalk, C.C., Dickey, T.D., 1990. The physical strength of marine snow and
855 its implications for particle disaggregation in the ocean. *Limnology and Oceanography* 35(7), 1415-
856 1428.

857 Alonso-González, I.J., Arístegui, J., Lee, C., Sanchez-Vidal, A., Calafat, A., Fabrés, J., Sangrá, P., Masqué, P.,
858 Hernández-Guerra, A., Benítez-Barríos, V., 2010. Role of slowly settling particles in the ocean carbon
859 cycle. *Geophysical Research Letters* 37, L13608, 10.1029/2010GL043827.

860 Alvarado Quiroz, N.G., Hung, C.-C., Santschi, P.H., 2006. Binding of thorium(IV) to carboxylate, phosphate
861 and sulfate functional groups from marine exopolymeric substances (EPS). *Marine Chemistry* 100(3-4),
862 337-353.

863 Arbic, B., Richman, J., Shriver, J., 2012. Global modeling of internal tides within an eddying ocean general
864 circulation model. *Oceanography* 25(2), 20-29.

865 Arístegui, J., Mendonça, A., Vilas, J.C., Espino, M., Polo, I., Montero, M.F., Martins, A., 2009. Plankton
866 metabolic balance at two North Atlantic seamounts. *Deep-Sea Research Part II* 56, 2646-2655.

867 Bashmachnikov, I., Mohn, C., Pelegrí, J.L., Martins, A., Jose, F., Machín, F., White, M., 2009. Interaction of
868 Mediterranean water eddies with Sedlo and Seine Seamounts, Subtropical Northeast Atlantic. *Deep
869 Sea Research Part II* 56, 2593-2605.

870 Behrenfeld, M., Falkowski, P., 1997. Photosynthetic rates derived from satellite-based chlorophyll
871 concentration. *Limnology and Oceanography* 42(1), 1-20.

872 Benitez-Nelson, C.R., Buesseler, K.O., Rutgers van der Loeff, M.M., Andrews, J., Ball, L., Crossin, G.,
873 Charette, M.A., 2001a. Testing a new small-volume technique for determining thorium-234 in
874 seawater. *Journal of Radioanalytical and Nuclear Chemistry* 248(3), 795-799.

875 Benitez-Nelson, C., Buesseler, K.O., Karl, D.M., Andrews, J., 2001b. A time-series study of particulate matter
876 export in the North Pacific Subtropical Gyre based on ^{234}Th : ^{238}U disequilibrium. *Deep-Sea Research I*
877 48, 2595-2611.

878 Berhane, I., Sternberg, R.W., Kineke, G.C., Milligan, T.G., Krancks, K., 1997. The variability of suspended
879 aggregates on the Amazon Continental Shelf. *Continental Shelf Research* 17(3), 267-285.

880 Bhat, S.G., Krishnaswamy, S., Lal, D., Rama, Moore, W.S., 1968. $^{234}\text{Th}/^{238}\text{U}$ ratios in the ocean. *Earth and*
881 *Planetary Science Letters* 5, 483-491.

882 Bidigare, R., Benitez-Nelson, C., Leonard, C.L., Quay, P.D., Parsons, M.L., Foley, D.G., Seki, M.P., 2003.
883 Influence of a cyclonic eddy on microheterotroph biomass and carbon export in the lee of Hawaii.
884 *Geophysical Research Letters* 30(6), 10.1029/2002GL016393.

885 Bory, A., Jeandel C., Leblond, N., Vangriesheim, A., Khripounoff, A., Beaufort, L., Rabouille, C., Nicolas, E.,
886 Tachikawa, K., Etcheber, H., Buat-Ménard, P., 2001. Downward particle fluxes within different
887 productivity regimes off the Mauritanian upwelling zone (EUMELI program). *Deep-Sea Research I*
888 48(10), 2251-2282.

889 Brust, J., Waniek, J.J., 2010. Atmospheric dust contribution to deep-sea particle fluxes in the subtropical
890 Northeast Atlantic. *Deep Sea Research I* 57(8), 988-998.

891 Buesseler, K., 1998. The decoupling of production and particulate export in the surface ocean. *Global*
892 *Biogeochemical Cycles* 12(2), 297-310.

893 Buesseler, K., Bacon, M.P., Cochran, J.K., Livingston, H.D., 1992. Carbon and nitrogen export during the
894 JGOFS North Atlantic Bloom experiment estimated from ^{234}Th : ^{238}U disequilibria. *Deep Sea Research*,
895 39(7), 1115–1137.

896 Buesseler, K.O., Benitez-Nelson, C.R., Moran, S.B., Burd, A., Charette, M., Cochran, J.K., Coppola, L., Fisher,
897 N.S., Fowler, S.W., Gardner, W.D., Guo, L.D., Gustafsson, Ø., Lamborg, C., Masque, P., Miquel, J.C.,
898 Passow, U., Santschi, P.H., Savoye, N., Stewart, G., Trull, T., 2006. An assessment of particulate organic
899 carbon to thorium-234 ratios in the ocean and their impact on the application of ^{234}Th as a POC flux
900 proxy. *Marine Chemistry* 100, 213–233.

901 Buesseler, K.O., Lamborg, C., Cai, P., Escoube, R., Johnson, R., Pike, S., Masque, P., McGillicuddy, D.,
902 Verdeny, E., 2008. Particle fluxes associated with mesoscale eddies in the Sargasso Sea. *Deep Sea*
903 *Research II* 55(10-13), 1426–1444.

904 Burd, A.B., Jackson, G.A., 2009. Particle aggregation. *Annual Review of Marine Science* 1, 65-90.

905 Chapman, D., Haidvogel, D., 1992. Formation of Taylor caps over a tall isolated seamount in a stratified
906 ocean. *Geophysical and Astrophysical Fluid Dynamics* 64(1-4), 31–65.

907 Chen, J., Edwards, R.L., Wasserburg, G.J., 1986. ^{238}U , ^{234}U and ^{232}Th in seawater. *Earth and Planetary Science*
908 *Letters* 80(3-4), 241–251.

909 Chiapello, I., Bergametti, G., 1995. An additional low layer transport of Sahelian and Saharan dust over the
910 north-eastern Tropical Atlantic. *Geophysical Research Letters* 22(23), 3191–3194.

911 Christiansen, B., Brand, T., Büntzow, M., Busecke, J., Coelho, R., Correia, S., Denda, A., Deniz, T., Jung, S.,
912 Kaufmann, M., Kieneke, A., Kiriakoulakis, K., Koppelman, R., Kuhnert, J., Kwasnitschka, T., Lamont, P.,
913 Martin, B., Montgomery, J., Peine, F., Piedade, A., Reichelt, T., Rieger, V., Schmidt, A., Stahl, H., Tiedke,
914 J., Truscheit, T., Turnewitsch, R., Unger, K., Vogel, S., Warneke-Cremer, C., 2011. Structure and
915 Function of Seamount Ecosystems in the Cape Verde Region, Northeast Atlantic - Cruise No. M79/3 -

916 September 24 - October 23, 2009 - Las Palmas (Spain) - Mindelo (Cape Verde). METEOR-Berichte,
917 M79/3, 53 pp., DFG-Senatskommission für Ozeanographie, DOI:10.2312/cr_m79_3

918 Clegg, S.L., Whitfield M., 1990. A generalized model for the scavenging of trace metals in the open ocean - I.
919 Particle cycling. Deep-Sea Research 37(5), 809-832.

920 Clegg, S.L., Whitfield, M., 1991. A generalized model for the scavenging of trace metals in the open ocean -
921 II. Thorium scavenging. Deep-Sea Research 38(1), 91-120.

922 Coale, K.H., Bruland, K.W., 1985. ^{234}Th : ^{238}U disequilibria within the California Current. Limnology and
923 oceanography 30(1), 22-33.

924 Coale, K.H., Bruland, K.W., 1987. Oceanic stratified euphotic zone as elucidated by ^{234}Th : ^{238}U disequilibria.
925 Limnology and Oceanography 32(1), 189-200.

926 De La Rocha, C.L., Passow, U., 2007. Factors influencing the sinking of POC and the efficiency of the
927 biological carbon pump. Deep-Sea Research II 54, 639-658.

928 Denda, A., Christiansen, B., 2014. Zooplankton distribution patterns at two seamounts in the subtropical
929 and tropical NE Atlantic. Marine Ecology 35, 159-179.

930 Denda, A., Mohn, C., Wehrmann, H., Christiansen, B., 2016. Microzooplankton and meroplanktonic larvae
931 at two seamounts in the subtropical and tropical NE Atlantic. Journal of the Marine Biological
932 Association of the United Kingdom, 1-27, doi: 10.1017/S0025315415002192.

933 Dower, J., Mackas, D., 1996. "Seamount effects" in the zooplankton community near Cobb Seamount.
934 Deep-Sea Research I 43(6), 837-858.

935 Ducklow, H., Steinberg, D., Buesseler, K.O., 2001. Upper ocean carbon export and the biological pump.
936 Oceanography 14(4), 50-58.

- 937 Durden, J.M., Bett, B.J., Jones, D.O.B., Huvenne, V.A.I., Ruhl, H.A., 2015. Abyssal hills - hidden source of
938 increased habitat heterogeneity, benthic megafaunal biomass and diversity in the deep sea. *Progress*
939 *in Oceanography* 137, 209-218.
- 940 Egbert, G.D., Erofeeva, S., 2002. Efficient inverse modeling of barotropic ocean tides. *Journal of*
941 *Atmospheric and Oceanic Technology* 19, 183-204.
- 942 Firing, E., Ranada, J., Caldwell, S., 1995. Processing ADCP data with the CODAS software system version 3.1.
943 User's manual. Joint Institute for Marine and Atmospheric Research, University of Hawaii, USA.
- 944 Fischer, G., Romero, O., Merkel, U., Donner, B., Iversen, M., Nowald, N., Ratmeyer, V., Ruhland, G., Klann,
945 M., Wefer, G., 2016. Deep ocean mass fluxes in the coastal upwelling off Mauritania from 1988 to
946 2012: variability on seasonal to decadal timescales. *Biogeosciences* 13(10), 3071-3090.
- 947 Fitzsimmons, J.N., Zhang, R., Boyle, E.A., 2013. Dissolved iron in the tropical North Atlantic Ocean. *Marine*
948 *Chemistry* 154, 87-99.
- 949 Garrett, C., Kunze, E., 2007. Internal tide generation in the deep ocean. *Annual Review of Fluid Mechanics*
950 39(1), 57-87.
- 951 Genin, A., 2004. Bio-physical coupling in the formation of zooplankton and fish aggregations over abrupt
952 topographies. *Journal of Marine Systems* 50(1-2), 3-20.
- 953 Gibson, C.H., Nabatov, V., Ozmidov, R., 1993. Measurements of turbulence and fossil turbulence near
954 Ampere seamount. *Dynamics of Atmospheres and Oceans* 19, 175-204.
- 955 Goldner, D.R., Chapman, D.C., 1997. Flow and particle motion induced above a tall seamount by steady and
956 tidal background currents. *Deep Sea Research I* 44(5), 719-744.
- 957 Guo, L., Hung, C.-C., Santschi, P.H., Walsh, I.D., 2002. ²³⁴Th scavenging and its relationship to acid
958 polysaccharide abundance in the Gulf of Mexico. *Marine Chemistry* 78, 103-119.

- 959 Hagen, E., 1985. A meandering intermediate front North-West off Cape Verde Islands. *Oceanographie*
960 *Tropicale* 20(1), 71–83.
- 961 Hagen, E., 2001. Northwest African upwelling scenario. *Oceanologica Acta* 24(S), S113-S128.
- 962 Hanel, R., John, H.-C., Meyer-Klaeden, O., Piatkowski, U., 2010. Larval fish abundance, composition and
963 distribution at Senghor Seamount (Cape Verde Islands). *Journal of Plankton Research* 32(11), 1541–
964 1556.
- 965 Hayward, T.L., 1994. The shallow oxygen maximum layer and primary production. *Deep-Sea Research I*
966 41(3), 559-574.
- 967 Hummon, J., Firing, E., 2003. A direct comparison of two RDI shipboard ADCPs: a 75-KHz Ocean surveyor
968 and a 150-kHz narrow band. *Journal of Atmospheric and Oceanic Technology* 20, 872–888.
- 969 Johnston, T.M.S., Rudnick, D.L., Carter, G.S., Todd, R.E., Cole, S.T., 2011. Internal tidal beams and mixing
970 near Monterey Bay. *Journal of Geophysical Research* 116, C03017.
- 971 Karl, D.M., Christian, J.R., Dore, J.E., Hebel, D.V., Letelier, R.M., Tupas, L.M., Winn, C.D., 1996. Seasonal and
972 interannual variability in primary production and particle flux at Station ALOHA. *Deep-Sea Research II*
973 43, 539-568.
- 974 Kiriakoulakis, K., Vilas, J.C., Blackbird, S.J., Aristegui, J., Wolff, G.A., 2009. Seamounts and organic matter—Is
975 there an effect? The case of Sedlo and Seine seamounts, Part 2. Composition of suspended particulate
976 organic matter. *Deep Sea Research II* 56(25), 2631–2645.
- 977 Lamb, K.G., 2004. Nonlinear interaction among internal wave beams generated by tidal flow over
978 supercritical topography. *Geophysical Research Letters* 31, L09313, doi:09310.01029/02003GL019393.

979 Lampitt, R.S., Boorman, B., Brown, L., Lucas, M., Salter, I., Sanders, R., Saw, K., Seeyave, S., Thomalla, S.J.,
980 Turnewitsch, R., 2008. Particle export from the euphotic zone: Estimates using a novel drifting
981 sediment trap, ^{234}Th and new production. *Deep-Sea Research I* 55(11), 1484-1502.

982 Lathuilière, C., Echevin, V., Lévy, M., 2008. Seasonal and intraseasonal surface chlorophyll-*a* variability
983 along the northwest African coast. *Journal of Geophysical Research* 113(C5), C05007,
984 doi:10.1029/2007JC004433.

985 Lavelle, J.W., Mohn, C., 2010. Motion, commotion, and biophysical connections at deep ocean seamounts.
986 *Oceanography* 23(1), 90–103.

987 Lázaro, C., Fernandes, M.J., Santos, A.M.P., Oliveira, P. 2005. Seasonal and interannual variability of surface
988 circulation in the Cape Verde region from 8 years of merged T/P and ERS-2 altimeter data. *Remote*
989 *Sensing of Environment*, 98(1), 45–62.

990 Legg, S., Huijts, K.M.H., 2006. Preliminary simulations of internal waves and mixing generated by finite
991 amplitude tidal flow over isolated topography. *Deep-Sea Research II* 53(1-2), 140–156.

992 Legg, S., Klymak, J., 2008. Internal hydraulic jumps and overturning generated by tidal flow over a tall steep
993 ridge. *Journal of Physical Oceanography* 38(9), 1949–1964.

994 Le Moigne, F.A.C., Villa-Alfagem, M., Sanders, R.J., Marsay, C., Henson, S., García-Tenorio, R., 2013. Export
995 of organic carbon and biominerals derived from ^{234}Th and ^{210}Po at the Porcupine Abyssal Plain. *Deep-*
996 *Sea Research I* 72, 88–101.

997 Lueck, R.G., Mudge, T.D., 1997. Topographically induced mixing around a shallow seamount. *Science* 276,
998 1831-1833.

999 Lutz, M.J., Caldeira, K., Dunbar, R.B., Behrenfeld, M.J., 2007. Seasonal rhythms of net primary production
1000 and particulate organic carbon flux to depth describe the efficiency of biological pump in the global
1001 ocean. *Journal of Geophysical Research* 112(C10), C10011, doi:10.1029/2006JC003706.

- 1002 Luyten, J., Pedlosky, J., Stommel, H., 1983. The ventilated thermocline. *Journal of Physical Oceanography*
1003 13, 292–309.
- 1004 MacKenzie, B.R., Leggett, W.C., 1993. Wind-based models for estimating the dissipation rates of turbulent
1005 energy in aquatic environments: empirical comparisons. *Marine Ecology Progress Series* 94, 207-216.
- 1006 Maiti, K., Buesseler, K.O., Pike, S.M., Benitez-Nelson, C., Cai, P., Chen, W., Cochran, K., Dai, M., Dehairs, F.,
1007 Gasser, B., Kelly, R.P., Masque, P., Miller, L., Miquel, J.C., Moran, S.B., Morris, P.J., Peine, F., Planchon,
1008 F., Renfro, A.A., Rutgers van der Loeff, M., Santschi, P., Turnewitsch, R., Waples, J.T., Xu, C., 2012.
1009 Intercalibration studies of short-lived thorium-234 in the water column and marine particles.
1010 *Limnology and Oceanography: Methods* 10, 631–644.
- 1011 Maiti, K., Benitez-Nelson, C.R., Bidigare, R., 2008. The influence of a mature cyclonic eddy on particle
1012 export. *Deep Sea Research II* 55, 1445–1460.
- 1013 Marshall, J., Adcroft, A., Hill, C., Perelman, L., Heisey, C., 1997. A finite-volume, incompressible Navier
1014 Stokes model for studies of the ocean on parallel computers. *Journal of Geophysical Research*
1015 102(C3), 5753-5766.
- 1016 Martínez-Marrero, A., Rodríguez-Santana, A., Hernández-Guerra, A., Fraile-Nuez, E., López-Laatzén, F.,
1017 Vélez-Belchí, P., Parrilla, G., 2008. Distribution of water masses and diapycnal mixing in the Cape
1018 Verde Frontal Zone. *Geophysical Research Letters* 35(7), L07609, doi:10.1029/2008GL033229.
- 1019 McCave, I.N., 1975. Vertical flux of particles in the ocean. *Deep-Sea Research* 22, 491–502.
- 1020 Meunier, T., Barton, E.D., Barreiro, B., Torres, R., 2012. Upwelling filaments off Cap Blanc: Interaction of the
1021 NW African upwelling current and the Cape Verde frontal zone eddy field? *Journal of Geophysical*
1022 *Research* 117(C8), 1–18.
- 1023 Michaels, A.F., Knap, A.H., 1996. Overview of the US JGOFS Bermuda Atlantic Time series Study and the
1024 Hydrostation S program. *Deep-Sea Research II* 43(2–3), 157–198.

- 1025 Mittelstaedt, E., 1983. The upwelling area off Northwest Africa—a description of phenomena related to
1026 coastal upwelling. *Progress in Oceanography* 12, 307–331.
- 1027 Mohn, C., White, M., 2010. Seamounts in a restless ocean: Response of passive tracers to sub-tidal flow
1028 variability. *Geophysical Research Letters* 37(15), pp.1–5.
- 1029 Mohn, C., Erofeeva, S., Turnewitsch, R., Christiansen, B., White, M., 2013. Tidal and residual currents over
1030 abrupt deep-sea topography based on shipboard ADCP data and tidal model solutions for three
1031 popular bathymetry grids. *Ocean Dynamics* 63(2-3), 195-208.
- 1032 Morris, K.J., Bett, B.J., Durden, J.M., Benoist, N.M.A., Huvenne, V.A.I., Jones, D.O.B., Robert, K., Ichino, M.C.,
1033 Wolff, G.A., Ruhl, H.A., 2016 (in press). Landscape-scale spatial heterogeneity in phytodetrital cover
1034 and megafauna biomass in the abyss links to modest topographic variation. *Scientific Reports*.
- 1035 Morris, P.J., Sanders, R., Turnewitsch, R., Thomalla, S., 2007. ²³⁴Th-derived particulate organic carbon
1036 export from an island-induced phytoplankton bloom in the Southern Ocean. *Deep-Sea Research II* 54,
1037 2208-2232.
- 1038 Mouriño, B., Fernández, E., Serret, P., Harbour, D., Sinha, B., Pingree, R., 2001. Variability and seasonality of
1039 physical and biological fields at the Great Meteor Tablemount (subtropical NE Atlantic). *Oceanologica*
1040 *Acta* 24(2), 1–20.
- 1041 Müller, B., Siedler, G., 1992. Multi-year current time series in the eastern North Atlantic Ocean. *Journal of*
1042 *Marine Research* 50, 63–98.
- 1043 Mullineau, L., Mills, S., 1997. A test of the larval retention hypothesis in seamount-generated flows. *Deep*
1044 *Sea Research I* 44(5), 745–770.
- 1045 Ohde, T., Siegel, H., 2010. Biological response to coastal upwelling and dust deposition in the area off
1046 Northwest Africa. *Continental Shelf Research* 30(9), 1108–1119.

- 1047 Onken, R., Klein, B., 1991. A model of baroclinic instability and waves between the ventilated gyre and the
1048 shadow zone of the North Atlantic Ocean. *Journal of Physical Oceanography* 21, 53–67.
- 1049 Owens, S.A., Buesseler, K.O., Sims, K.W.W., 2011. Re-evaluating the ^{238}U -salinity relationship in seawater:
1050 Implications for the ^{238}U - ^{234}Th disequilibrium method. *Marine Chemistry* 127(1-4), 31–39.
- 1051 Owens, S.A., Pike, S., Buesseler, K.O., 2015. Thorium-234 as a tracer of particle dynamics and upper ocean
1052 export in the Atlantic Ocean. *Deep-Sea Research II* 116, 42-59.
- 1053 Passow, U., Murray, J.W., Balistrieri, L., Alldredge, A.L., 2006. Organic carbon to ^{234}Th ratios of marine
1054 organic matter. *Marine Chemistry* 100(3-4), 323–336.
- 1055 Pastor, M.V., Pelegrí, J.L., Hernández-Guerra, A., Fonta, J., Salata, J., Emelianov, M., 2008. Water and
1056 nutrient fluxes off Northwest Africa. *Continental Shelf Research* 28(7), 915–936.
- 1057 Peine, F., Turnewitsch, R., Mohn, C., Reichelt, T., Springer, B., Kaufmann, M., 2009. The importance of tides
1058 for sediment dynamics in the deep sea - Evidence from the particulate-matter tracer ^{234}Th in deep-
1059 sea environments with different tidal forcing. *Deep Sea Research I* 56(7), 1182–1202.
- 1060 Ratmeyer, V., Balzer, W., Bergametti, G., Chiapello, I., Fischer, G., Wyputta, U., 1999a. Seasonal impact of
1061 mineral dust on deep-ocean particle flux in the eastern subtropical Atlantic Ocean. *Marine Geology*
1062 159(1-4), 241–252.
- 1063 Ratmeyer, V., Fischer, G., Wefer, G., 1999b. Lithogenic particle fluxes and grain size distributions in the
1064 deep ocean off northwest Africa: Implications for seasonal changes of aeolian dust input and
1065 downward. *Deep-Sea Research* 46, 1289–1337.
- 1066 Resplandy, L., Martin, A.P., LeMoigne, F., Martin, P., Aquilina, A., Mémery, L., Lévy, M., Sanders, R., 2012.
1067 How does dynamical spatial variability impact ^{234}Th -derived estimates of organic export? *Deep-Sea*
1068 *Research I* 68, 24–45.

1069 Rodriguez y Baena, A.M., Metian, M., Teyssié, J.-L., De Broyer, C., Warnau, M., 2006. Experimental evidence
1070 for ^{234}Th bioaccumulation in three Antarctic crustaceans: Potential implications for particle flux
1071 studies. *Marine Chemistry* 100, 354-365.

1072 Rogers, 1994. The Biology of Seamounts. *Advances in Marine Biology* 30, 305–350.

1073 Rowden, A.A., Dower, J.F., Schlacher, T.A., Consalvey, M., Clark, M.R., 2010. Paradigms in seamount
1074 ecology: fact, fiction and future. *Marine Ecology* 31 (S1), 226–241.

1075 Rutgers van der Loeff, M., Sarin, M.M., Baskaran, M., Benitez-Nelson, C., Buesseler, K.O., Charette, M., Dai,
1076 M., Gustafsson, Ö., Masque, P., Morris, P.J., Orlandini, K., Rodriguez y Baena, A., Savoye, N., Schmidt,
1077 S., Turnewitsch, R., Vöge, I., Waples., J.T., 2006. A review of present techniques and methodological
1078 advances in analyzing ^{234}Th in aquatic systems. *Marine Chemistry* 100(3-4), 190–212.

1079 Rutgers van der Loeff, M. M., Moore, W.S., 1999. Determination of natural radioactive tracers. In: *Methods*
1080 *of Seawater Analysis*. Eds.: K. Grasshoff, K. Kremling, M. Ehrhardt. Weinheim, Wiley-VCH, 365-397.

1081 Santschi, P.H., Murray, J.W., Baskaran, M., Benitez-Nelson, C.R., Guo, L.D., Hung, C.-C., Lamborg, C., Moran,
1082 S.B., Passow, U., Roy-Barman, M., 2006. Thorium speciation in seawater. *Marine Chemistry* 100(3-4),
1083 250–268.

1084 Savoye, N., Benitez-Nelson, C., Burd, A.B., Cochran, J.K., Charette, M., Buesseler, K.O., Jackson, G.A., Roy-
1085 Barman, M., Schmidt, S., Elskens, M., 2006. ^{234}Th sorption and export models in the water column: A
1086 review. *Marine Chemistry* 100(3-4), 234–249.

1087 Schlitzer, R., 2002. Interactive analysis and visualization of geoscience data with Ocean Data View.
1088 *Computers and Geoscience* 28(10), 1211-1218.

1089 Siedler, G., Paul, U., 1991. Barotropic and baroclinic tidal currents in the eastern basins of the North
1090 Atlantic. *Journal of Geophysical Research* 96(C12), 22259–22271.

- 1091 Siedler, G., Zangenberg, N., 1992. Seasonal changes in the tropical Atlantic circulation: Observation and
1092 simulation of the Guinea Dome. *Journal of Geophysical Research* 97(C1), 703–715.
- 1093 Stramma, L., G. Siedler (1988). Seasonal changes in the North-Atlantic sub-tropical gyre. *Journal of*
1094 *Geophysical Research* 93(C7), 8111-8118.
- 1095 Stramma, L., Brandt, P., Schafstall, J., Schott, F., Fischer, J., Körtzinger, A., 2008. Oxygen minimum zone in
1096 the North Atlantic south and east of the Cape Verde Islands. *Journal of Geophysical Research* 113, 1-
1097 15.
- 1098 Stramma, L., Hüttl, S., Schafstall, J., 2005. Water masses and currents in the upper tropical northeast
1099 Atlantic off northwest Africa. *Journal of Geophysical Research* 110(C12), C12006,
1100 doi:10.1029/2005JC002939.
- 1101 Troupin, C., Mason, E., Beckers, J.-M., Sangra, P., 2012. Generation of the Cape Ghir upwelling filament: A
1102 numerical study. *Ocean Modelling* 41, 1-15.
- 1103 Turnewitsch, R., Falahat, S., Nycander, J., Dale, A., Scott, R.B., Furnival, D., 2013. Deep-sea fluid and
1104 sediment dynamics—Influence of hill- to seamount-scale seafloor topography. *Earth-Science Reviews*
1105 127, 203–241.
- 1106 Turnewitsch, R. Springer, B.M., Kiriakoulakis, K., Vilas, J.C., Arístegui, J., Wolff, G., Peine, F., Werk, S., Graf,
1107 G., Waniek, J.J., 2007. Determination of particulate organic carbon (POC) in seawater: The relative
1108 methodological importance of artificial gains and losses in two glass-fiber-filter-based techniques.
1109 *Marine Chemistry* 105(3-4), 208–228.
- 1110 Turnewitsch, R., Reyss, J.-L., Nycander, J., Waniek, J.J., Lampitt, R.S., 2008. Internal tides and sediment
1111 dynamics in the deep sea—Evidence from radioactive $^{234}\text{Th}/^{238}\text{U}$ disequilibria. *Deep-Sea Research I*
1112 55(12), 1727–1747.

- 1113 Turnewitsch, R., Springer, B., 2001. Do bottom mixed layers influence ^{234}Th dynamics in the abyssal near-
1114 bottom water column? *Deep-Sea Research I* 48, 1279–1307.
- 1115 Turnewitsch, R., Lahajnar, N., Haeckel, M., Christiansen, B., 2015. An abyssal hill fractionates organic and
1116 inorganic matter in deep-sea surface sediments. *Geophysical Research Letters* 42,
1117 doi:10.1002/2015GL065658.
- 1118 Vangriesheim, A., Bournot-Marec, C., Fontan, A., 2003. Flow variability near the Cape Verde frontal zone
1119 (subtropical Atlantic Ocean). *Oceanologica Acta* 26, 149–159.
- 1120 Verdeny, E., Masqué, P., Maiti, K., Garcia-Orellana, J., Bruach, J.M., Mahaffey, C., Benitez-Nelson, C.R.,
1121 2008. Particle export within cyclonic Hawaiian lee eddies derived from Pb-210-Po-210 disequilibrium.
1122 *Deep Sea Research II* 55(10-13), 1461–1472.
- 1123 Vilas, J.C., Arístegui, J., Kiriakoulakis, K., Wolff, G.A., Espino, M., Polo, I., Montero, M.F., Mendonça, A.,
1124 2009. Seamounts and organic matter - Is there an effect? The case of Sedlo and Seine Seamounts:
1125 Part1. Distributions of dissolved and particulate organic matter. *Deep-Sea Research II* 56, 2618-2630.
- 1126 Waterhouse, A.F., MacKinnon, J.A., Nash, J.D., Alford, M.H., Kunze, E., Simmons, H.L., Polzin, K.L., St
1127 Laurent, L.C., Sun, O.M., Pinkel, R., Talley, L.D., Whalen, C.B., Huussen, T.N., Carter, G.S., Fer, I.,
1128 Waterman, S., Garabato, A. C.N., Sanford, T.B., Lee, C.M., 2014. Global patterns of diapycnal mixing
1129 from measurements of the turbulent dissipation rate. *Journal of Physical Oceanography* 44(7), 1854-
1130 1872.
- 1131 Watling, L., Guinotte, J., Clark, M.R., Smith, C.R., 2013. A proposed biogeography of the deep ocean floor.
1132 *Progress in Oceanography* 111, 91–112.
- 1133 Wessel, P., Sandwell, D., Kim, S., 2010. The global seamount census. *Oceanography* 23(1), 24-33.
- 1134 Whalen, C.B., Talley, L.D., MacKinnon, J.A., 2012. Spatial and temporal variability of global ocean mixing
1135 inferred from Argo profiles. *Geophysical Research Letters* 39, L18612, doi:10.1029/2012GL053196.

1136 White, M., Mohn, C., 2004. Seamounts: a review of physical processes and their influence on the seamount
1137 ecosystem. Oasis Report: http://epic.awi.de/37314/17/OASIS_Oceanography.pdf.

1138 Yamamouro, M., Kayanne, H., 1995. Rapid direct determination of organic carbon and nitrogen in
1139 carbonate-bearing sediments with a Yanaco MT-5 CHN analyser. *Limnology and Oceanography* 40,
1140 1001-1005.

1141 Zenk, W., Klein, B., Schröder, M., 1991. Cape Verde frontal zone. *Deep-Sea Research* 38(S1), S505-S530.

1142

1143 **Figure captions**

1144

1145 Fig. 1. (a) Map of the wider study area. NEC: North Equatorial Current; CVFZ: Cape Verde Frontal Zone. N-
1146 Ref: northern reference (far-field) site; S-Ref: southern reference (far-field) site. White box: location of
1147 Senghor Seamount. White rectangle line: area for which the near-surface currents are shown in Fig. 2a,b.
1148 Inset: ellipse of the clockwise-rotating current vector of the barotropic tide near S-Ref for the duration of
1149 the cruise, capturing two spring and two neap tides (extracted with hourly resolution from the TPXO
1150 barotropic tide model; Egbert and Erofeeva, 2002). (b) Swath-bathymetric map of Senghor Seamount. Grey
1151 circles and numbers: ^{234}Th sampling; white circles and letters: only hydrography.

1152

1153 Fig. 2. (a) AVISO-derived surface currents during September 2009. Bold isobaths: outlines of Sal island (S)
1154 and Boa Vista island (B). Areas surrounded by dashed white lines: approximate regions where the initial
1155 downward semidiurnal internal-tide beams that are generated on the upper slopes of Senghor Seamount
1156 reflect from the sea surface (also see Fig. S3). White circles: locations of N-Ref and S-Ref. Area surrounded
1157 by white rectangle line: area shown in (c) and (d). (b) Same as (a), but for October 2009. (c) Map of net
1158 primary productivity (NPP) in September 2009 as derived from the Vertically Generalized Productivity
1159 Model (VGPM; Behrenfeld and Falkowski, 1997). White approximately concentric lines: approximate
1160 outline of Senghor Seamount. White star symbols: sampling sites. White arrows: approximate (hand-
1161 drawn) AVISO-derived surface currents. The area that is surrounded by a thin white dashed line and
1162 emanates from the seamount indicates what could be a 'banner cloud' of seamount-enhanced NPP on the
1163 downstream side of the seamount. (d) Same as (c), but for October 2009. The detail of the approximate
1164 hand-drawn currents labelled 'ADCP' is derived from the VM-ADCP survey as shown in Fig. 3.

1165

1166 Fig. 3. Composite picture of ADCP-derived currents at different water levels at Senghor Seamount. The data
1167 set has not been de-tided. Isobaths: 200 m (centre), 500 m, 1000 m, 2000 m and 3000 m. Sampling stations
1168 as in Fig. 1b. Upper two plots: white dashed lines delineate the approximate regions of increased tidally-

1169 driven kinetic-energy dissipation (and turbulent-diffusive mixing); areas ('R') surrounded by dotted white
1170 lines: approximate regions where the initially upgoing seamount-generated semidiurnal internal-tide
1171 beams are thought to reflect from the sea surface (see black lines in Fig. 4b for beam paths).

1172

1173 Fig. 4. (a) Top: barotropic tidal current speed near S-Ref as derived from the TPXO model (Egbert and
1174 Erofeeva, 2002); horizontal bars labelled '²³⁴Th': time intervals during which the vast majority of ²³⁴Th
1175 samples was collected. Centre: VM-ADCP-derived E-W current-speed component (eastward: positive
1176 values) for the ship time at Senghor Seamount in 2009; dotted lines: identical phases of near-inertial
1177 oscillations. Bottom: corresponding VM-ADCP-derived N-S current-speed component (northward: positive
1178 values). Dashed boxes: time intervals for which detailed ADCP time series are shown in Fig. 5-7. (b,c) N-S
1179 transect of numerically modelled kinetic-energy dissipation resulting from interactions of semidiurnal
1180 barotropic tidal flow over Senghor Seamount. (b) Whole seamount; (c) topmost 800 m of the seamount.
1181 The results are time-averaged over 3.5 tidal cycles and for a 2D model set-up. Vertical dashed lines:
1182 approximate locations of the sampling stations on the northern and southern mid slopes (N-Slope and S-
1183 Slope). Horizontal black dashed line in (c): lower boundary of the 'export layer' at the seamount. Black
1184 (white) solid lines in (b): paths of the initially upward (downward) beams of the semidiurnal internal tide
1185 that is generated on the uppermost northern and southern slopes of the seamount. The geometry of the
1186 internal-tide beams in the wider study area is shown in Fig. S3 of the Online Supplement.

1187

1188 Fig. 5. VM-ADCP time series between Senghor Seamount and N-Ref. Left column: cruise M79/3 of RV
1189 Meteor in October 2009; right column: cruise 446 of RV Poseidon in February 2013. (a,b) E-W component,
1190 u , of the horizontal current velocity (positive values: eastward). (c,d) N-S component, v , of the horizontal
1191 current velocity (positive values: northward). (e,f) Magnitude of the horizontal current velocity that results
1192 from u and v . (g,h) Direction of the resulting current in degrees clockwise from N (N: $360^\circ = 0^\circ$). (i,j) Current
1193 speed and direction of the barotropic tide (derived from the TPXO model of Egbert and Erofeeva (2002)).

1194 Numbers above (g) and (h) relate to points in time (tidal phases) of the MITgcm-derived internal tides in
1195 Fig. S3.

1196

1197 Fig. 6. Representative VM-ADCP time series at Senghor Seamount. The approximate locations of the ship
1198 are indicated at the bottom of the plot. (a) Current speed and direction of the barotropic tide (derived from
1199 the TPXO model of Egbert and Erofeeva (2002)). (b) E-W component, u , of the horizontal current velocity.
1200 (c) N-S component, v , of the horizontal current velocity. (d) Magnitude of the horizontal current velocity
1201 that results from u and v . (e) Direction of the resulting current in degrees clockwise from N (N: $360^\circ = 0^\circ$).
1202 Note the emergence of the layered internal-wave structure in current directions after day 288.7 (dashed-
1203 line box) when barotropic tidal current speeds peak at $> 4.5 \text{ cm s}^{-1}$ during their semidiurnal cycles.

1204

1205 Fig. 7. Same as Fig. 6, but for the time interval of the transition from Senghor Seamount to S-Ref and
1206 further south to the Boa Vista Seamount. Note the layered internal-wave structure in current directions
1207 (dashed-line box) and speeds while barotropic tidal current speeds peak at $> 4.5 \text{ cm s}^{-1}$ during their
1208 semidiurnal cycles. Also note that these internal waves became less obvious after the ship had left the
1209 seamount on day 290.85 while barotropic tidal current speeds still peaked at $> 4.5 \text{ cm s}^{-1}$ during their
1210 semidiurnal cycles.

1211

1212 Fig. 8. Same as Fig. 6, but for a representative VM-ADCP time series at Senghor Seamount during cruise 446
1213 of RV Poseidon in February 2013. Arrows above plot (d) indicate directions of the ship's movements during
1214 a NNW excursion from the summit (first two arrows) and the repeat WSW-ENE transects across the summit
1215 (all other arrows). Note the prominent layered internal-wave structure in current directions and speeds
1216 throughout the time series when barotropic tidal current speeds peak at $> 4.5 \text{ cm s}^{-1}$ during their
1217 semidiurnal cycles.

1218

1219 Fig. 9. Composite N-S (left) and E-W (right) hydrographic sections across the summit of Senghor Seamount.
1220 Each plot displays salinity (shaded background), potential temperature (solid lines: °C) and dissolved oxygen
1221 (dashed lines: mg O₂ L⁻¹). CTD station numbers used to produce these plots are displayed above their cast
1222 locations in each plot. Created in ODV with VG-gridding interpolation (Schlitzer, 2002). The bathymetry was
1223 constructed by interpolating between station bottom depths, which were determined via a swath
1224 multibeam survey carried out during the cruise (Fig. 1b).

1225

1226 Fig. 10. Profiles of total ²³⁴Th activity (A_{Th}^t ; circles), ²³⁸U activity (A_U ; triangles), mass density of water (σ_θ ;
1227 solid line) and dissolved oxygen (dashed line) at the N-Ref (top-left), S-Ref (top-right) and Summit (bottom).
1228 σ_θ and dissolved-oxygen data have not been included in the S-Ref profile due to an equipment malfunction.
1229 Error bars for the A_{Th}^t and A_U data are one standard deviation.

1230

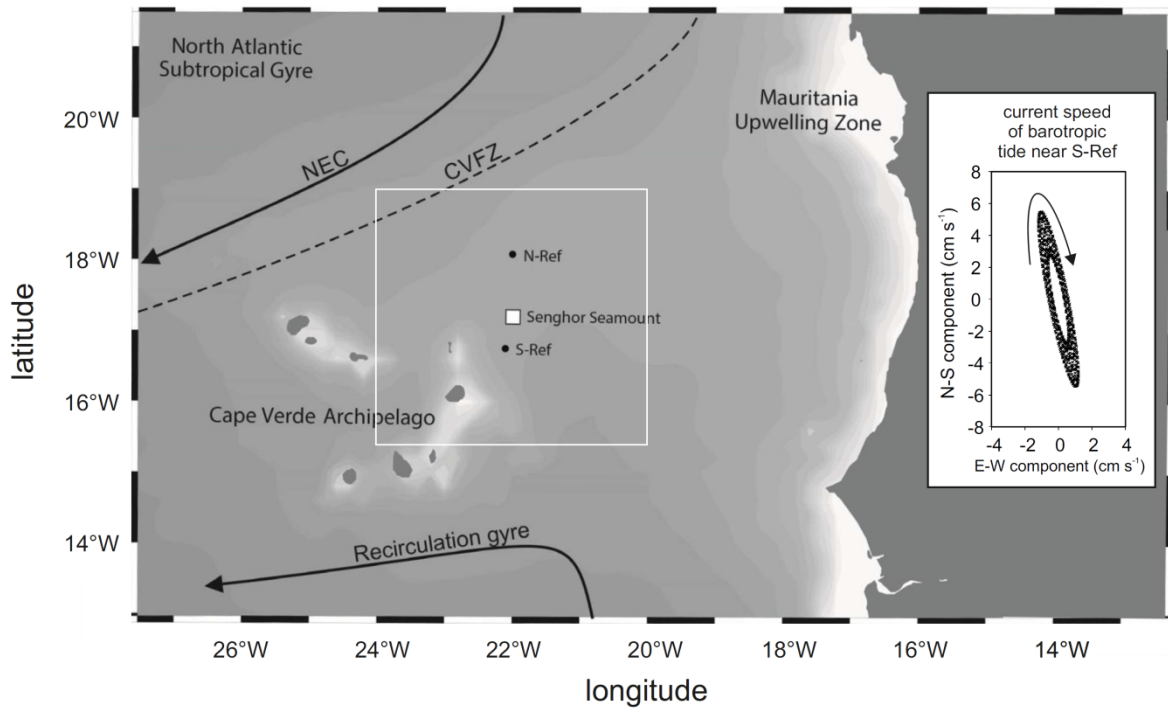
1231 Fig. 11. Same as Fig. 10, but for the W-Slope (top-left), E-Slope (top-right), N-Slope (bottom-left) and S-
1232 Slope (bottom-right).

1233

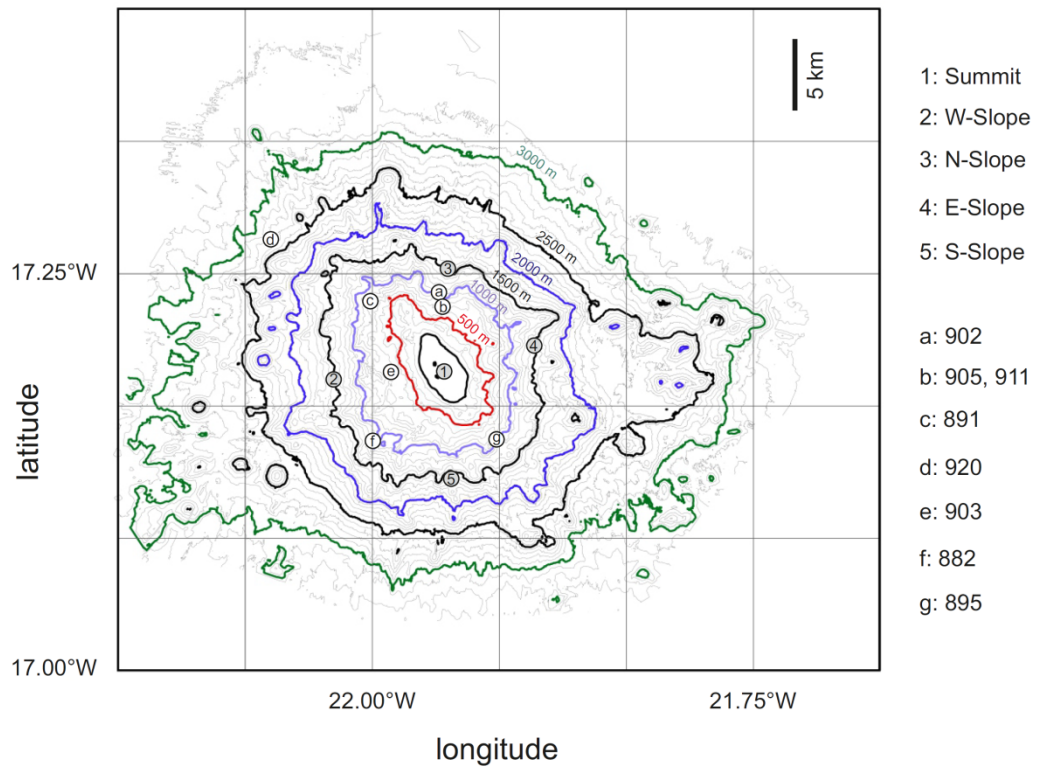
1234 Fig. 12. (a) Export fluxes of ²³⁴Th. Results for two different ways of calculating the fluxes are shown.
1235 (b) Export fluxes of POC. Results for four different ways of calculating the fluxes are shown. N-Ref is not
1236 viewed as a suitable reference site and separated from the other station results by the vertical dashed line.
1237 S-Ref was a suitable reference site for the seamount stations. Horizontal arrows below abscissa: E-Slope
1238 and N-Slope are viewed as sites that are located approximately upstream of S-Slope and W-Slope,
1239 respectively. Upward arrows indicate probable underestimates. Bidirectional arrow with '?': here, it is
1240 unclear whether there is an under- or overestimate. Error bars: \pm one propagated standard deviation.

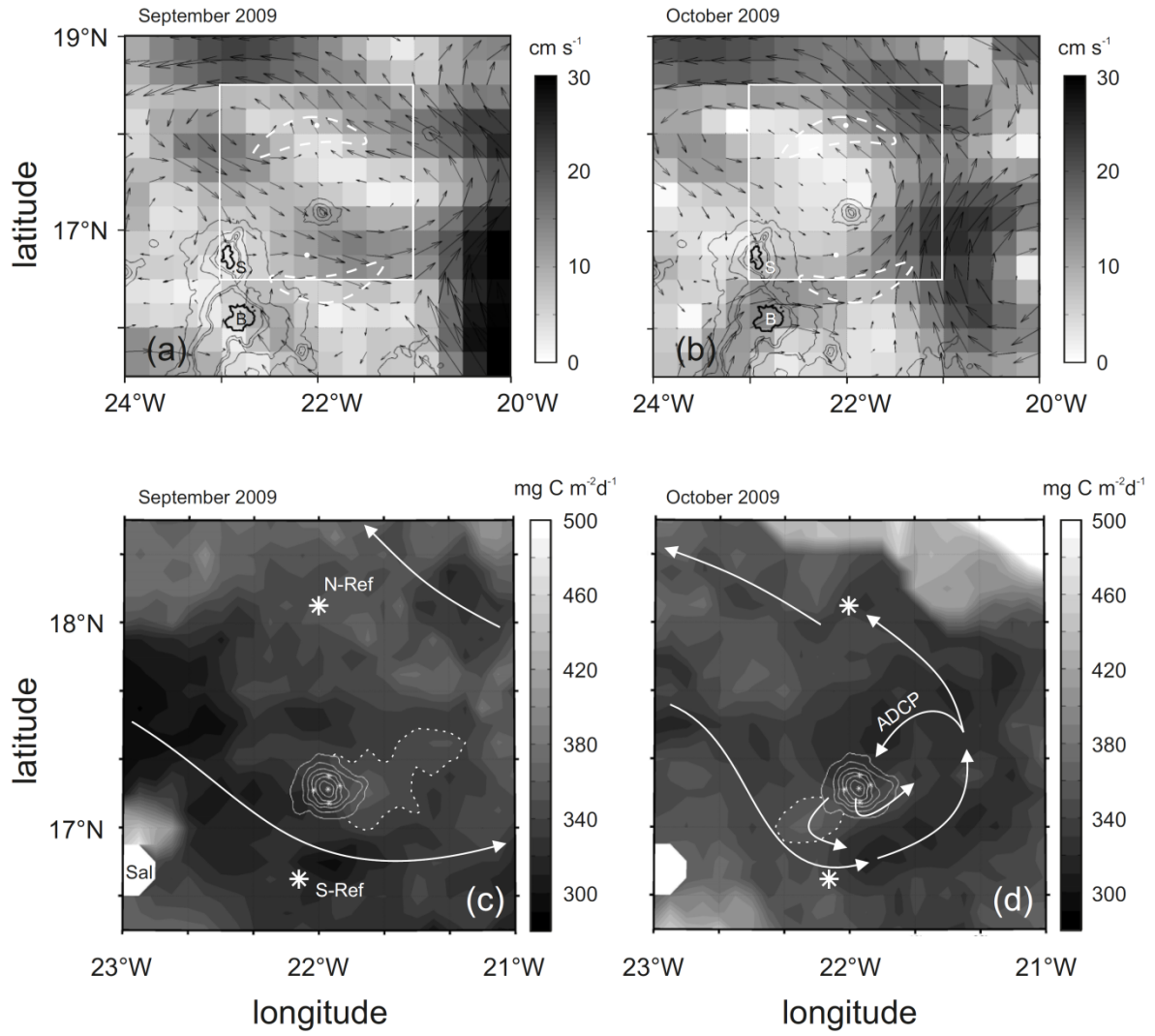
1241

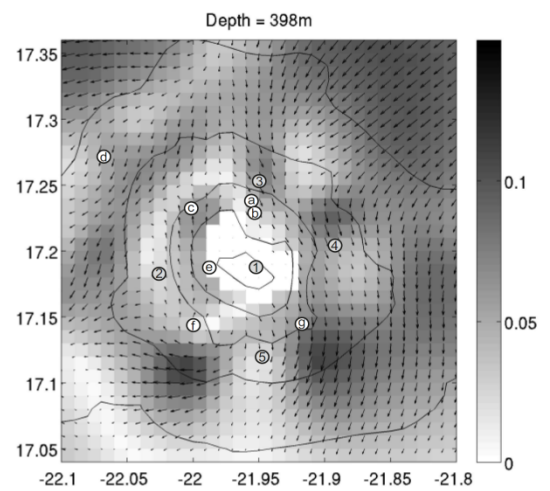
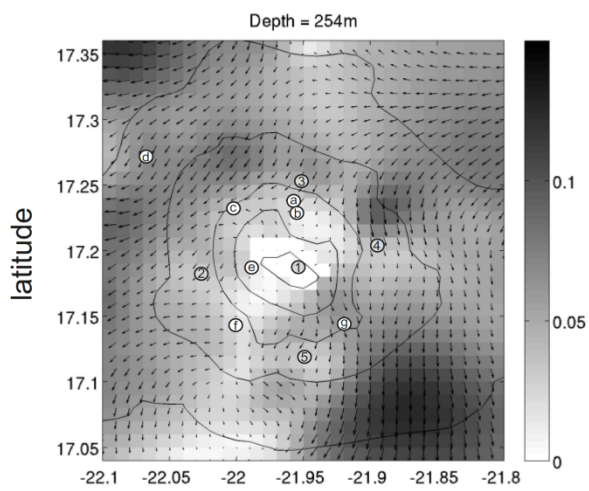
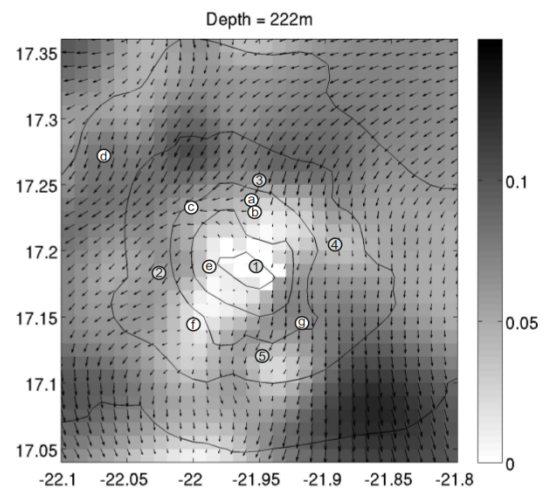
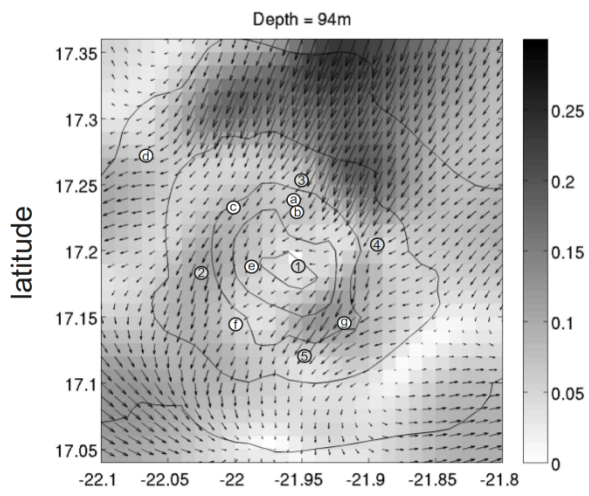
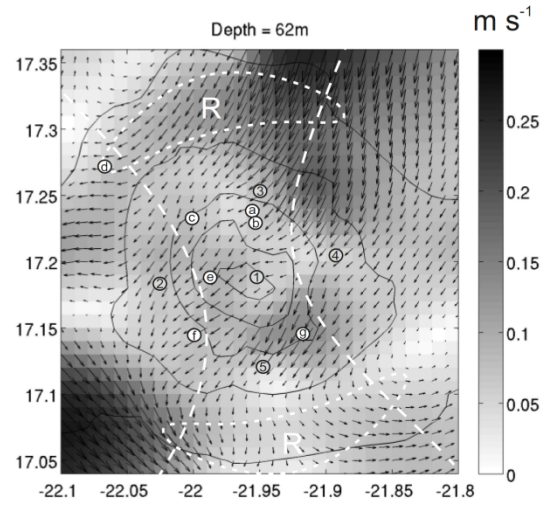
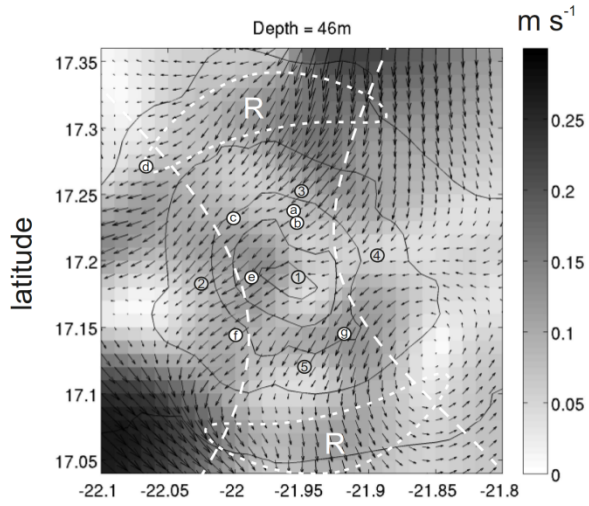
(a)



(b)

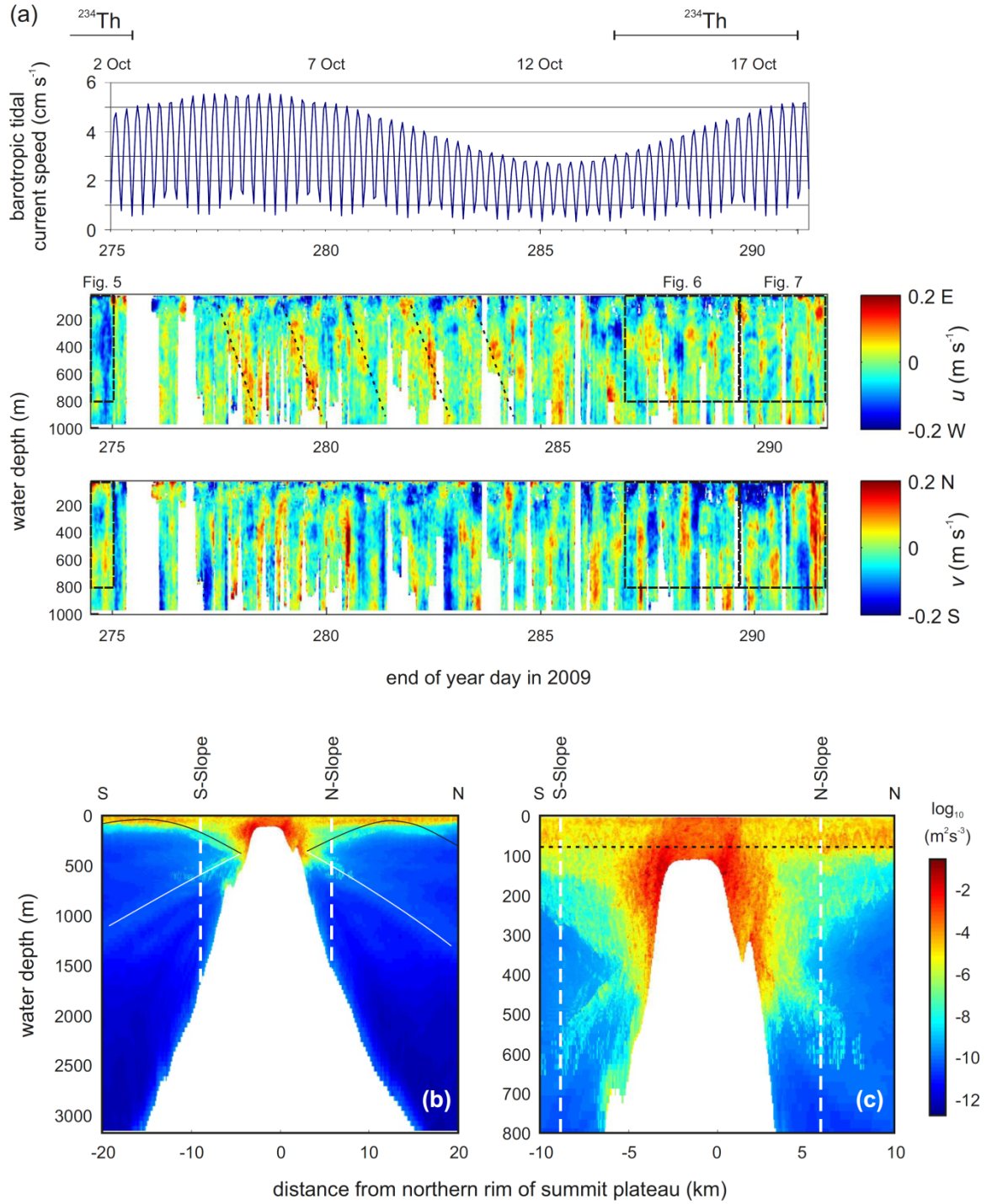


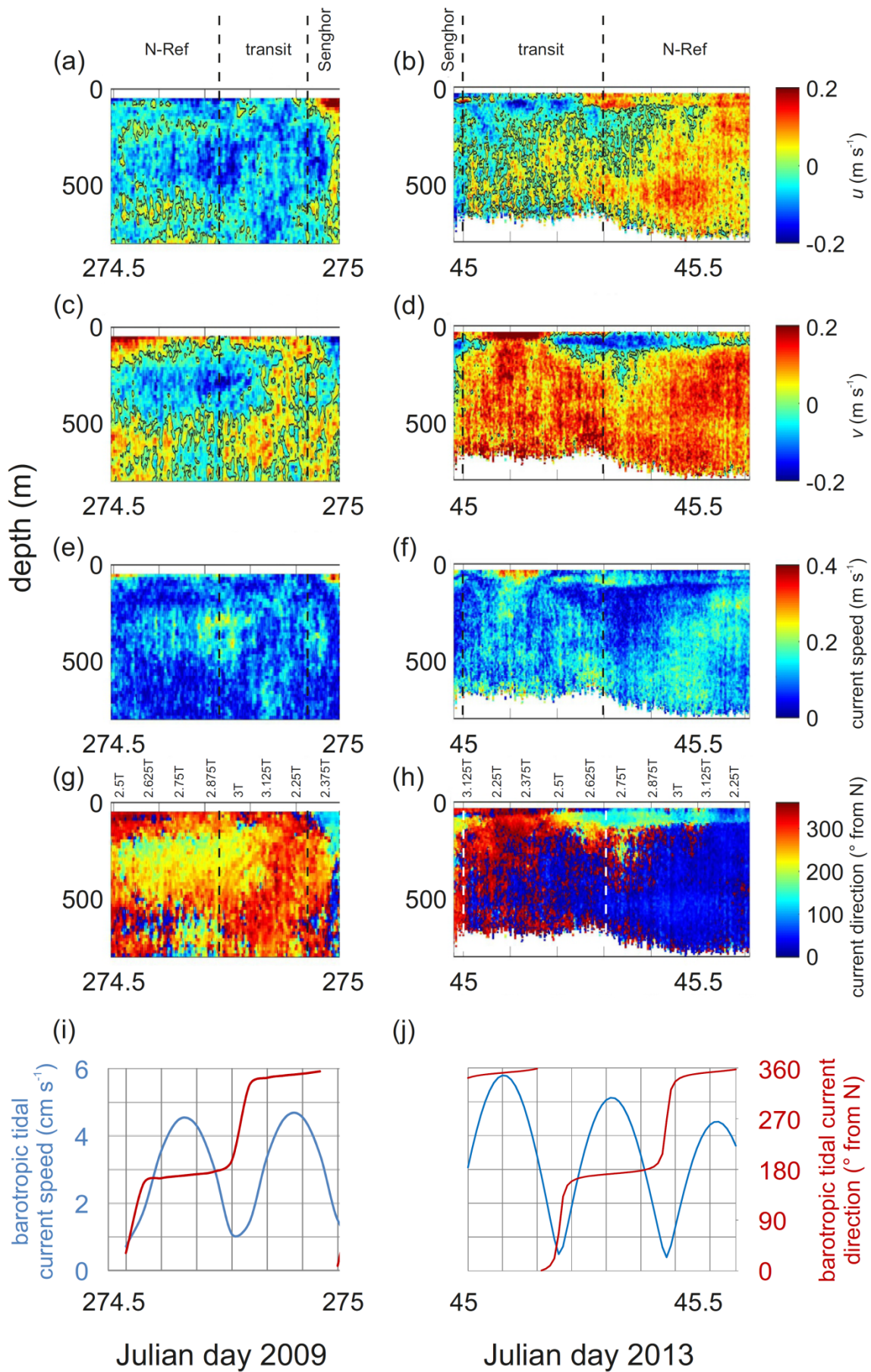


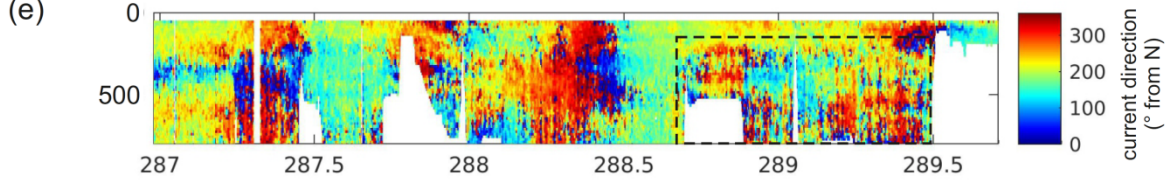
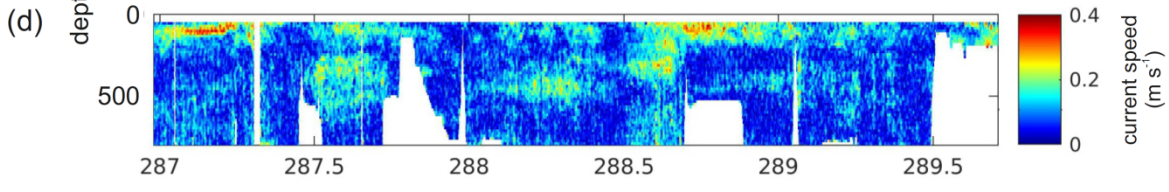
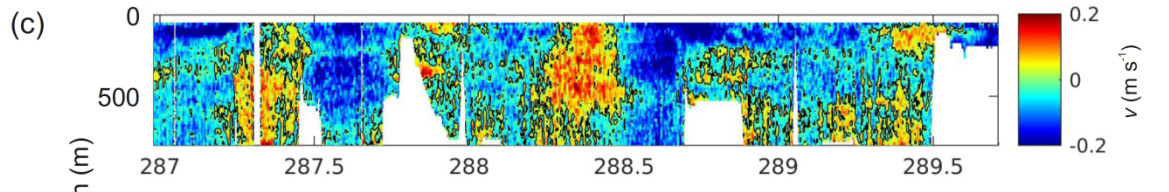
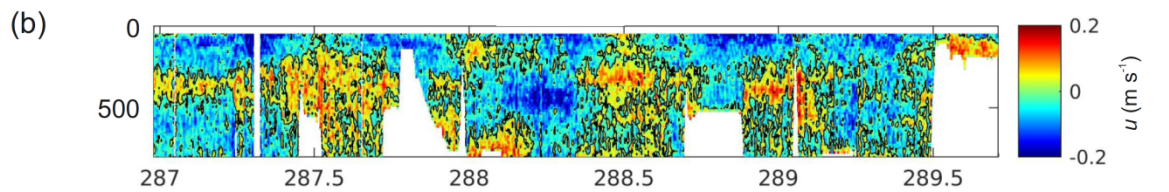
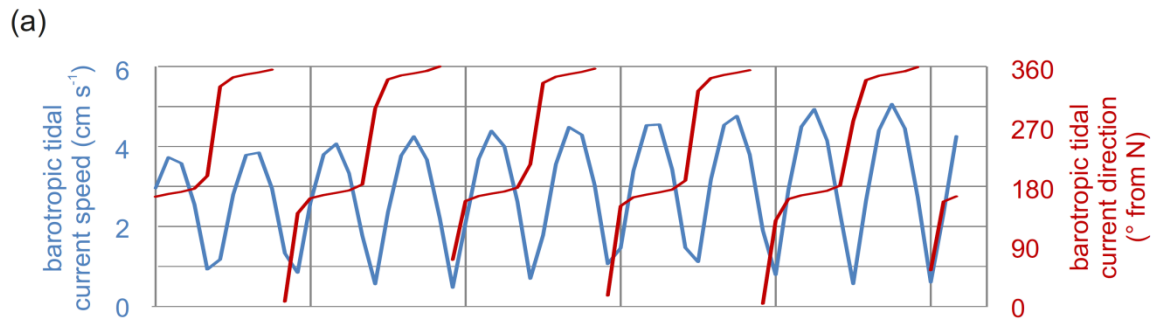


longitude

longitude

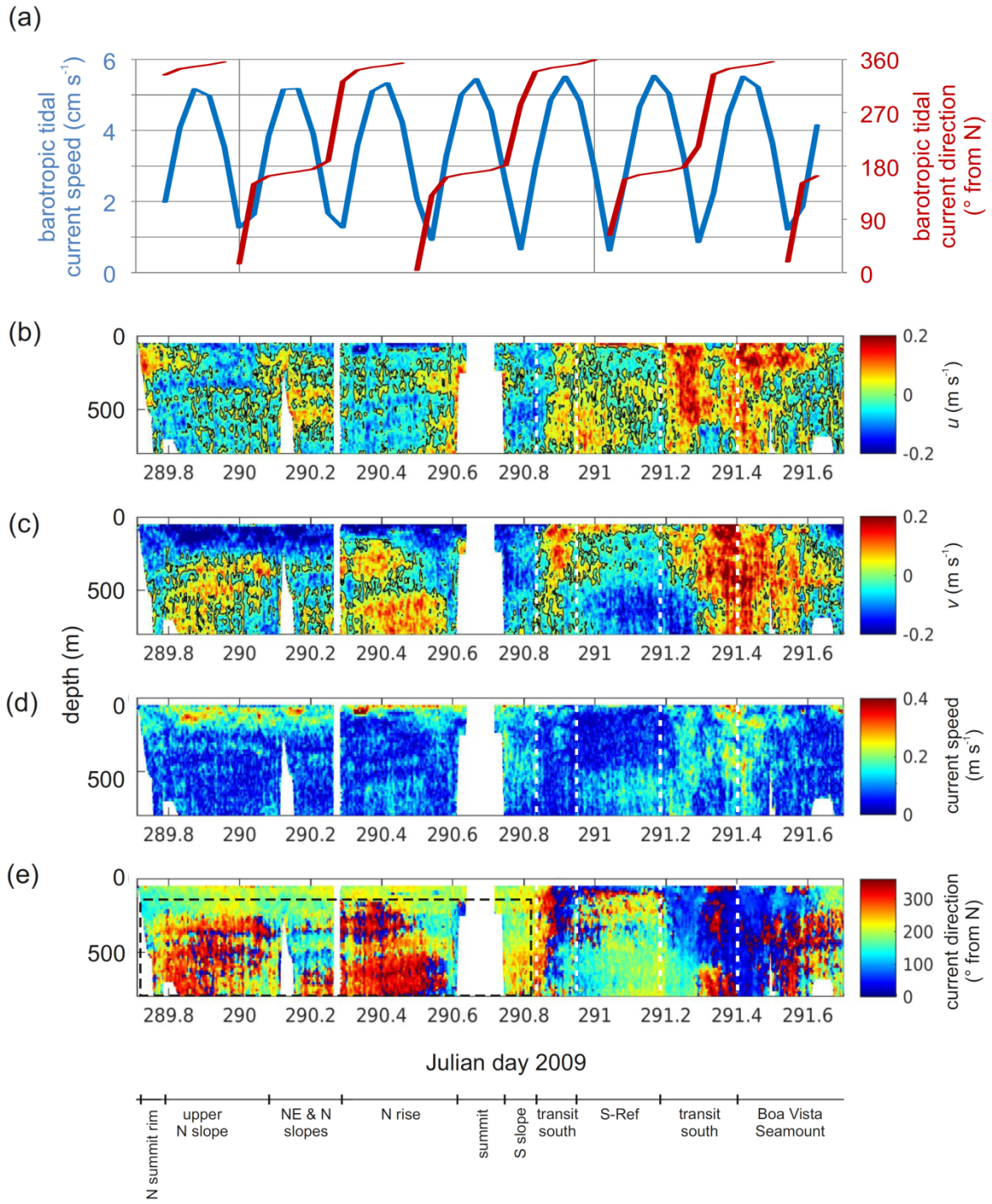


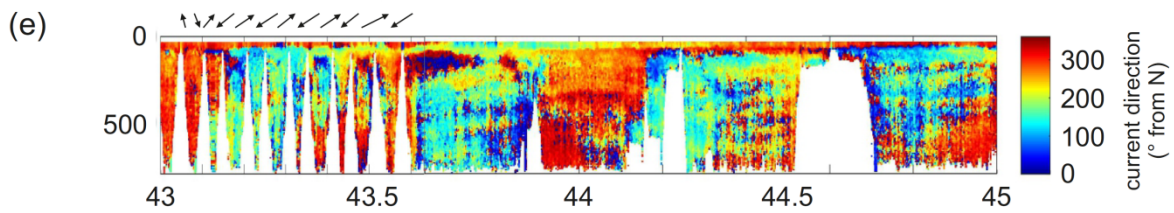
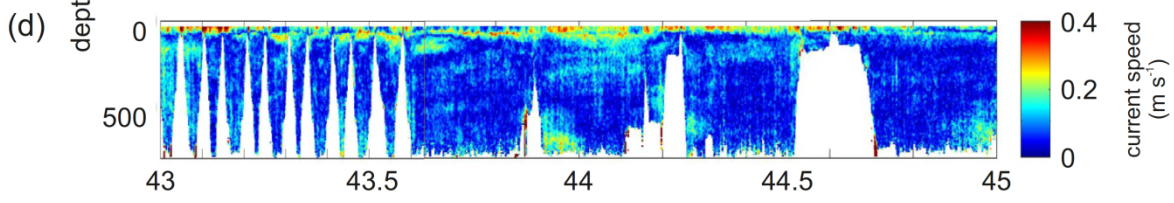
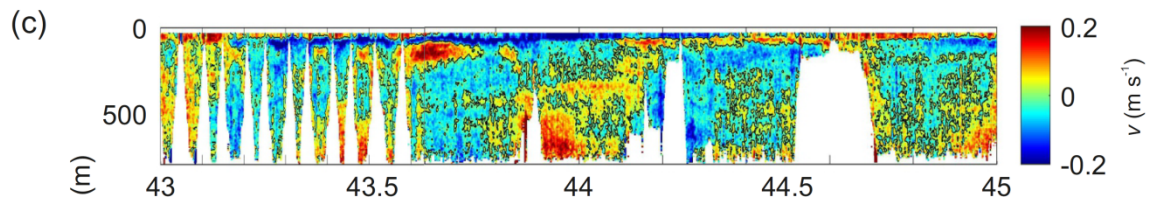
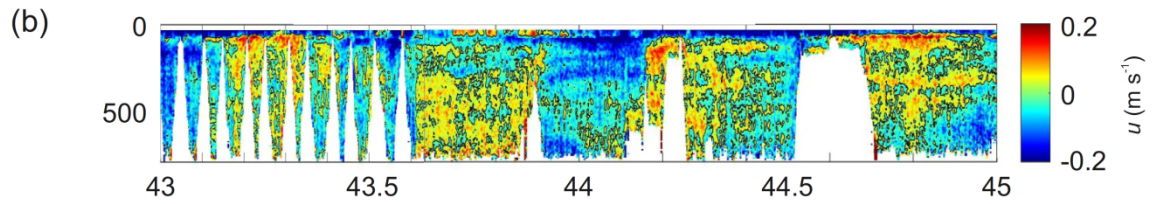
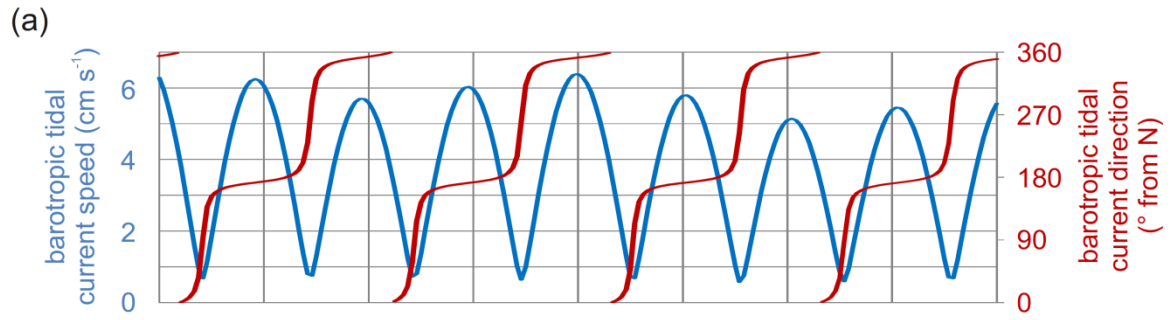




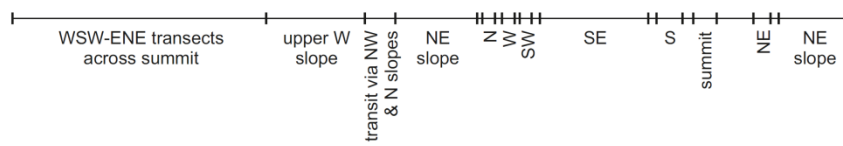
Julian day 2009

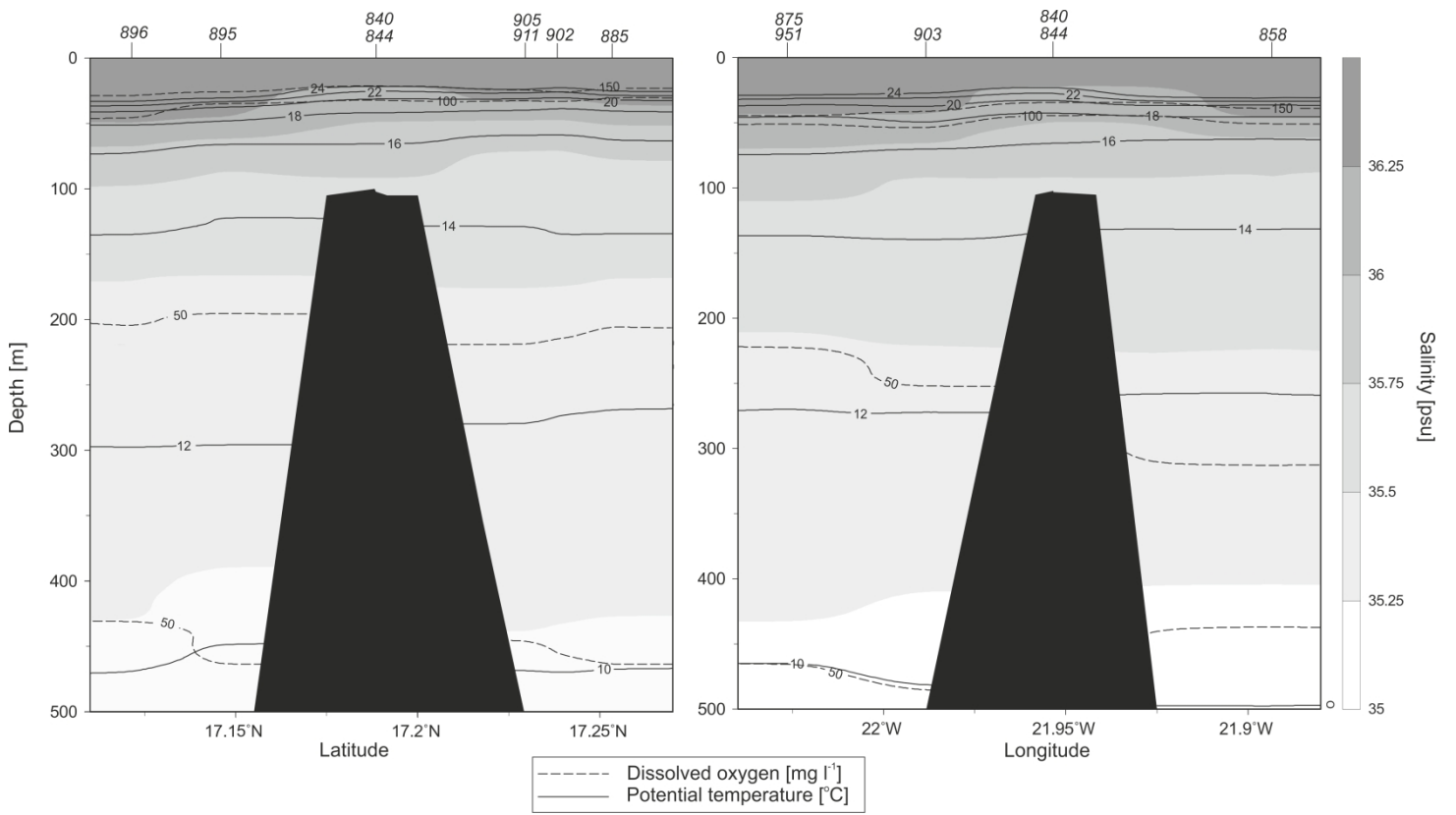
deeper NW slopes W Slope W rise upper N slope upper NE slope upper N slope N summit rim upper N slope SW slope W rise upper N slope N Slope S Slope E Slope upper N slope S summit rim W summit rim

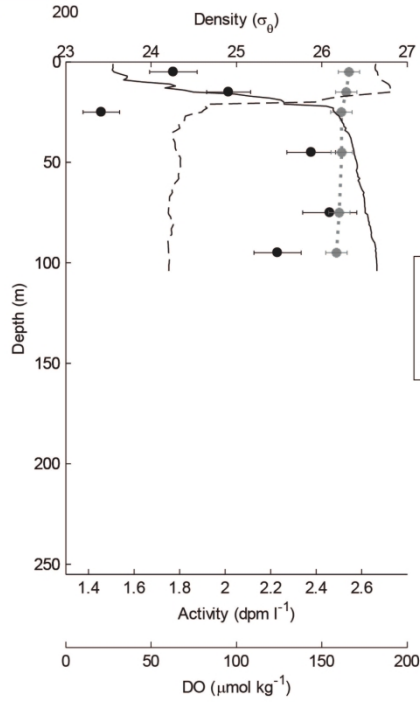
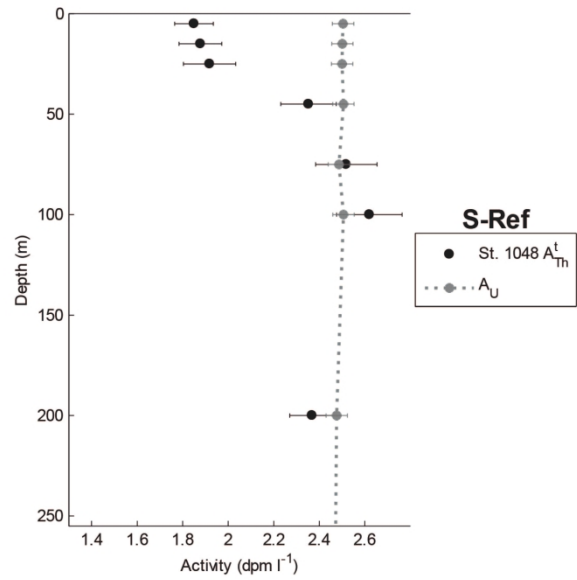
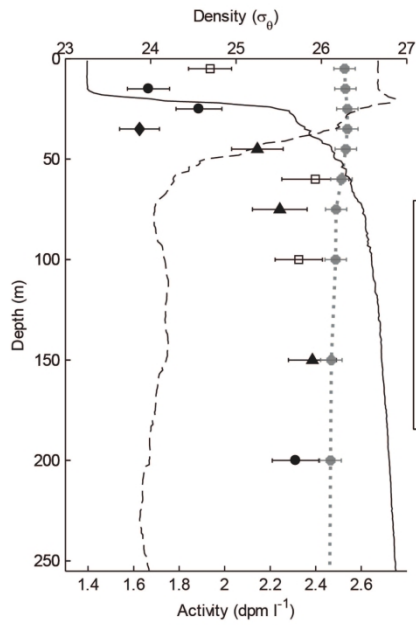


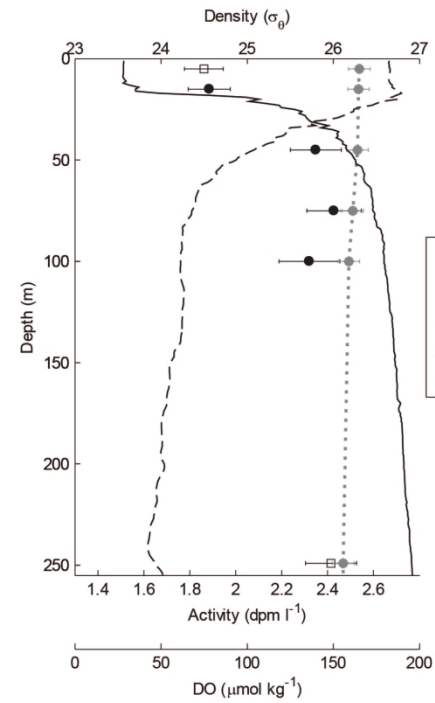
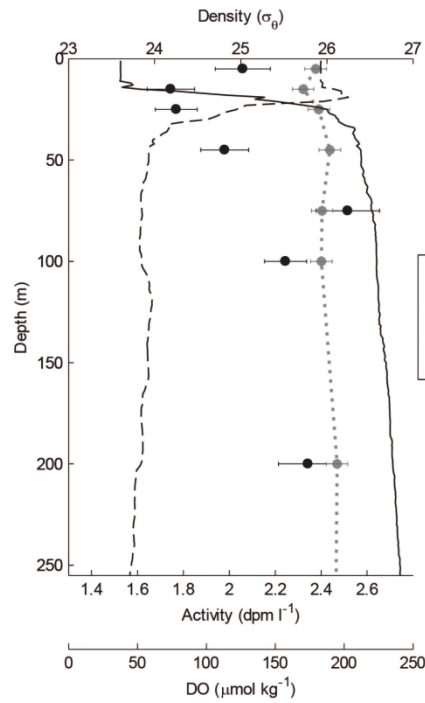
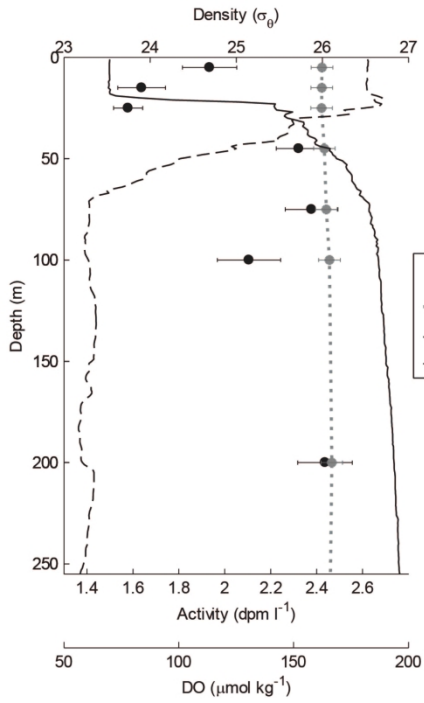
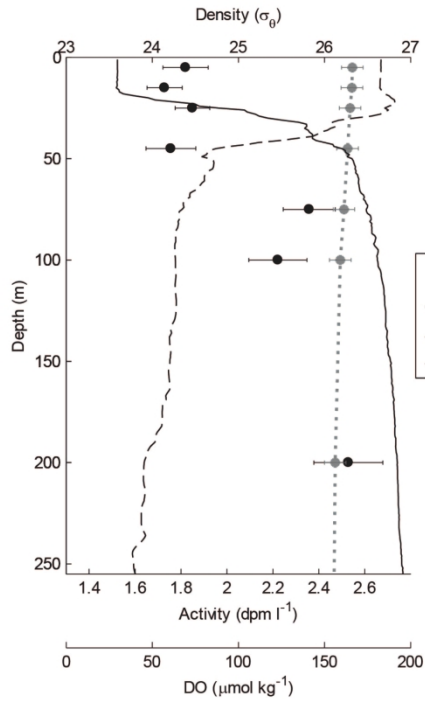


Julian day 2013









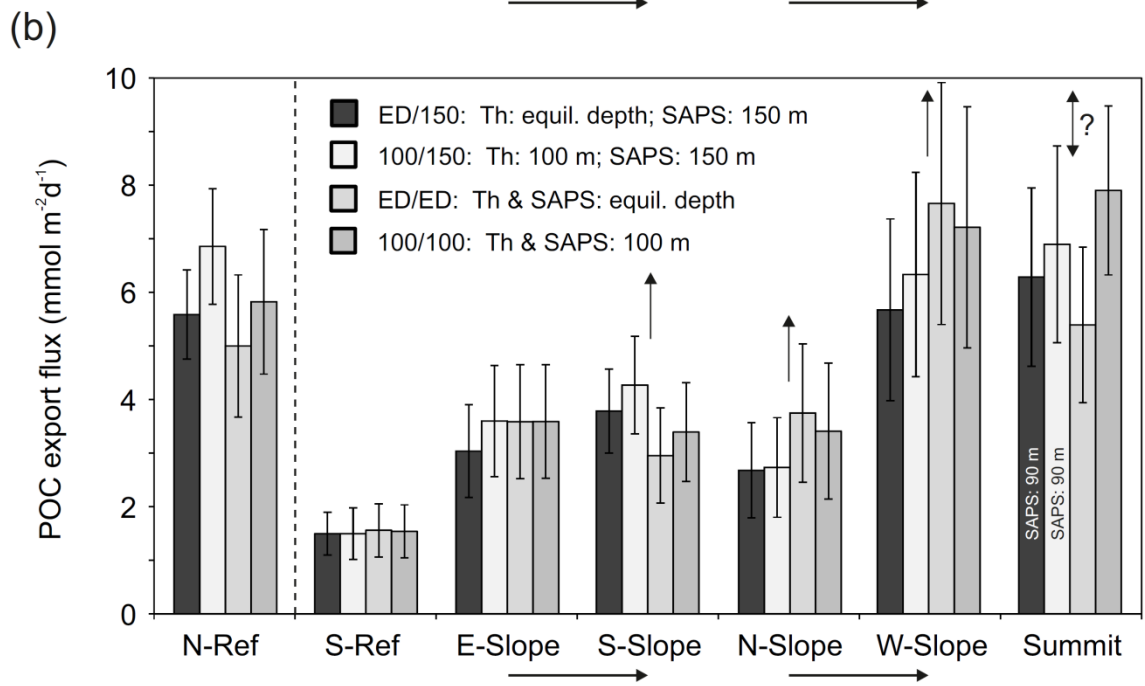
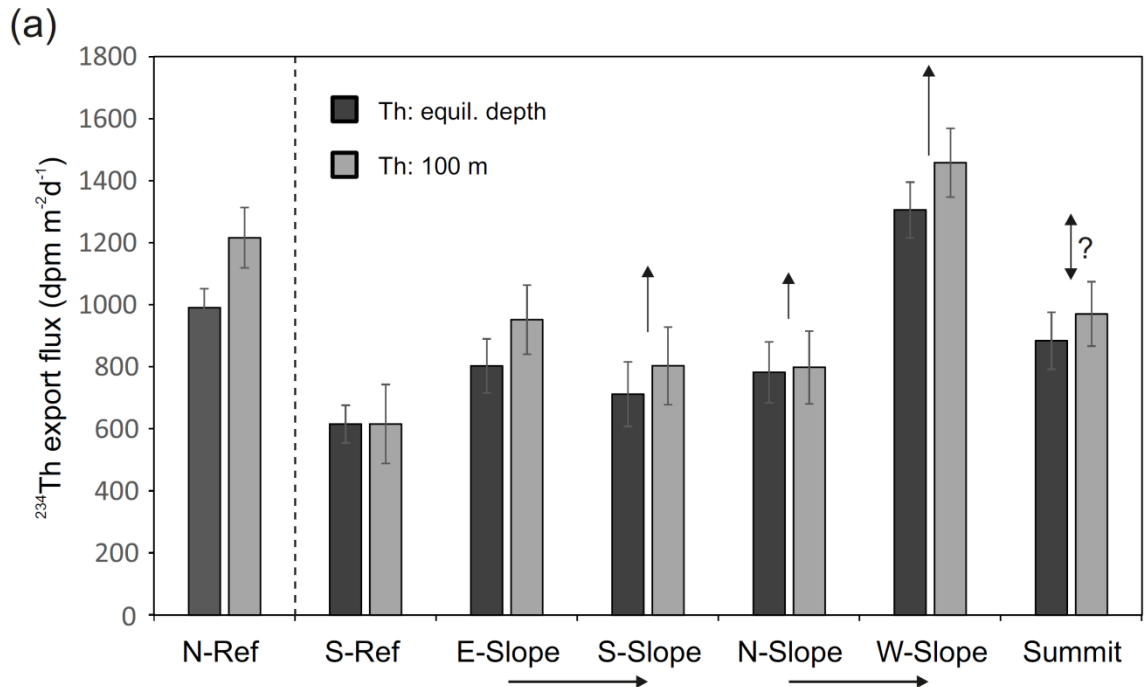


Table 1. Sampling-site locations, sampling devices, and sampling depths. SAPS: large-volume Stand-Alone Pumping System.

Site	station	Latitude (°N)	Longitude (°W)	Water depth at seafloor (m)	Sampling device	Sampling depths (m)
Northern reference (N-Ref)	801	18.0858	21.9998	3295	Bottles	15, 25, 200
	803	18.0828	21.9993	3295	SAPS	150
	808	18.0838	22.0007	3295	Bottles	5, 60, 100
					SAPS	32 ^a
	812	18.0820	22.0015	3295	Bottles	35, 1400 ^b
813	18.0833	21.9998	3295	Bottles	45, 75, 150	
Northern slope (N-Slope)	885	17.2533	21.9503	1575	SAPS	150
	1020	17.2532	21.9512	1555	Bottles	5, 15, 25, 45, 75, 100, 200
	1039	17.2533	21.9508	1570	SAPS	50
Summit (Summit)	840	17.1883	21.9533	100	Bottles	5, 15, 25, 45, 75, 95
					SAPS	50, 90
Western slope (W-Slope)	875	17.1833	22.0267	1520	SAPS	150
	1001	17.1840	22.0270	1535	Bottles	5, 15, 25, 45, 75, 100, 200
	1002	17.1840	22.0270	1535	SAPS	50
Eastern slope (E-Slope)	858	17.2050	21.8933	1550	SAPS	150
	1028	17.2045	21.8948	1485	Bottles	5, 15, 25, 45, 75, 100, 200
	1029	17.2047	21.8947	1500	SAPS	50
Southern slope (S-Slope)	896	17.1212	21.9482	1635	SAPS	150
	998	17.1212	21.9490	1645	Bottles	5, 249
	999	17.1210	21.9488	1640	Bottles	15, 45, 75, 100
SAPS					50	
Southern reference (S-Ref)	1048	16.7502	22.1005	3375	Bottles	5, 15, 25, 45, 75, 100, 200
					SAPS	50, 150

^a SAPS cast accidentally hoisted up from 50 m to 15 m during pumping. Sampling depth given as mid-point (32 m).

^b station, site and depth for replicate sampling

Table 2. Radioactivities of ^{238}U (A_U) and total ^{234}Th (A_{Th}^t), expressed as disintegrations per minute per litre of seawater (dpm L^{-1}). Uncertainties are given as one propagated standard deviation (1SD).

Station	Site	Sample depth (m)	A_U (dpm L^{-1}) ^a	A_U : 1SD (dpm L^{-1}) ^a	A_{Th}^t (dpm L^{-1})	A_{Th}^t : 1SD (dpm L^{-1})
808	N-Ref	5	2.527	0.047	1.94	0.09
801	N-Ref	15	2.530	0.047	1.67	0.09
801	N-Ref	25	2.539	0.047	1.89	0.10
812	N-Ref	35	2.539	0.047	1.63	0.09
813	N-Ref	45	2.532	0.047	2.14	0.11
808	N-Ref	60	2.513	0.047	2.40	0.15
813	N-Ref	75	2.490	0.047	2.24	0.12
808	N-Ref	100	2.488	0.047	2.33	0.10
813	N-Ref	150	2.468	0.047	2.39	0.11
801	N-Ref	200	2.465	0.047	2.31	0.10
812	N-Ref	1396	2.436	0.047	2.45	0.13
812	N-Ref	1398	2.436	0.047	2.43	0.13
812	N-Ref	1400	2.436	0.047	2.24	0.10
812	N-Ref	1402	2.436	0.047	2.30	0.16
812	N-Ref	1404	2.436	0.047	2.44	0.22
1020	N-Slope	5	2.376	0.047	2.06	0.12
1020	N-Slope	15	2.322	0.047	1.75	0.10
1020	N-Slope	25	2.390	0.047	1.77	0.09
1020	N-Slope	45	2.438	0.047	1.98	0.10
1020	N-Slope	75	2.404	0.047	2.52	0.14
1020	N-Slope	100	2.401	0.047	2.24	0.09
1020	N-Slope	200	2.469	0.047	2.34	0.13
840	Summit	5	2.544	0.047	1.77	0.10
840	Summit	15	2.532	0.047	2.02	0.10
840	Summit	25	2.511	0.047	1.46	0.08
840	Summit	45	2.513	0.047	2.38	0.11
840	Summit	75	2.502	0.047	2.46	0.12
840	Summit	95	2.489	0.047	2.23	0.10
1001	W-Slope	5	2.546	0.047	1.82	0.10
1001	W-Slope	15	2.544	0.047	1.73	0.08
1001	W-Slope	25	2.536	0.047	1.85	0.08
1001	W-Slope	45	2.525	0.047	1.76	0.11
1001	W-Slope	75	2.509	0.047	2.36	0.11
1001	W-Slope	100	2.493	0.047	2.22	0.13
1001	W-Slope	200	2.472	0.047	2.53	0.15
1028	E-Slope	5	2.423	0.047	1.93	0.12
1028	E-Slope	15	2.423	0.047	1.64	0.10
1028	E-Slope	25	2.422	0.047	1.58	0.06
1028	E-Slope	45	2.434	0.047	2.32	0.10
1028	E-Slope	75	2.442	0.047	2.38	0.12
1028	E-Slope	100	2.456	0.047	2.11	0.14
1028	E-Slope	200	2.466	0.047	2.44	0.12
998	S-Slope	5	2.538	0.047	1.86	0.08
999	S-Slope	15	2.535	0.047	1.88	0.09
999	S-Slope	45	2.531	0.047	2.35	0.11
999	S-Slope	75	2.509	0.047	2.43	0.12
999	S-Slope	100	2.492	0.047	2.32	0.13
998	S-Slope	249	2.468	0.047	2.41	0.11
1048	S-Ref	5	2.505	0.047	1.85	0.08
1048	S-Ref	15	2.502	0.047	1.88	0.09
1048	S-Ref	25	2.500	0.047	1.92	0.11
1048	S-Ref	45	2.506	0.047	2.35	0.12
1048	S-Ref	75	2.487	0.047	2.52	0.13
1048	S-Ref	100	2.507	0.047	2.62	0.14
1048	S-Ref	200	2.477	0.047	2.37	0.10

^a Calculated from the relationship between ^{238}U and salinity given by Owens et al. (2011).

Table 3. Radioactivities of ^{234}Th in SAPS-collected particulate matter (A_{Th}^{p}), expressed in terms of dpm per litre of filtered seawater. Uncertainties are given as one propagated standard deviation (1SD). Mesh: nominal pore size of 53 μm ; GF/F: nominal pore size of 0.7 μm , i.e., the data correspond to particles in the nominal size fraction 0.7-53 μm . GF/F data are corrected for ^{234}Th sorption (see Section 2.2.2.2 for details).

Station	Site	Filter type	Depth (m)	A_{Th}^{p} (dpm L ⁻¹)	A_{Th}^{p} : 1SD (dpm L ⁻¹)
808	<i>N-Ref</i>	mesh	32	0.023	0.001
808	<i>N-Ref</i>	GF/F	32	0.206	0.059
803	<i>N-Ref</i>	mesh	150	0.013	0.001
803	<i>N-Ref</i>	GF/F	150	0.161	0.017
1039	<i>N-Slope</i>	mesh	50	0.036	0.002
885	<i>N-Slope</i>	mesh	150	0.032	0.005
840	<i>Summit</i>	mesh	50	0.071	0.002
840	<i>Summit</i>	GF/F	50	0.044	0.016
840	<i>Summit</i>	mesh	90	0.019	0.002
840	<i>Summit</i>	GF/F	90	0.106	0.007
1002	<i>W-Slope</i>	mesh	50	0.024	0.001
875	<i>W-Slope</i>	mesh	150	0.009	0.000
875	<i>W-Slope</i>	GF/F	150	0.123	0.012
1029	<i>E-Slope</i>	mesh	50	0.023	0.001
858	<i>E-Slope</i>	mesh	150	0.015	0.001
858	<i>E-Slope</i>	GF/F	150	0.227	0.023
999	<i>S-Slope</i>	mesh	50	0.021	0.001
896	<i>S-Slope</i>	mesh	150	0.012	0.001
1048	<i>S-Ref</i>	mesh	50	0.015	0.001
1048	<i>S-Ref</i>	mesh	150	0.014	0.001

Table 4. Estimates of ^{234}Th export fluxes, POC / Th ratios in $> 53 \mu\text{m}$ particles, and POC export fluxes. Uncertainties are given as one propagated standard deviation (1SD).

Site	Lower boundary depth of export layer ^a	^{234}Th export	1SD	POC / ^{234}Th ^b	1SD	POC export ^e	1SD
	(m)	(dpm m ⁻² d ⁻¹)		($\mu\text{mol dpm}^{-1}$)		(mmol m ⁻² d ⁻¹)	
<i>N-Ref</i>	60	990	61	3.63 ^c	1.32 ^c	5.58	0.83
	100	1216	97	5.63	0.76	6.84	1.08
						4.99	1.33
						5.81	1.35
<i>N-Slope</i>	75	783	98	5.1	1.87	2.67	0.88
	100	799	117	3.42	1.05	2.73	0.93
						3.74	1.29
						3.40	1.27
<i>Summit</i>	75	884	92	2.96	1.01	6.27	1.66
	100	971	104	7.10 ^d	1.73 ^d	6.89	1.83
						5.38	1.45
						7.89	1.58
<i>W-Slope</i>	75	1306	90	5.55	1.73	5.66	1.70
	100	1458	111	4.34	1.26	6.32	1.90
						7.65	2.26
						7.20	2.25
<i>E-Slope</i>	75	803	87	3.75	1.05	3.03	0.86
	100	952	111	3.77	1.00	3.59	1.04
						3.58	1.06
						3.58	1.06
<i>S-Slope</i>	75	712	104	3.13	1.11	3.78	0.78
	100	803	125	5.31	0.77	4.26	0.91
						2.95	0.88
						3.39	0.92
<i>S-Ref</i>	75	616	61	2.56	0.63	1.49	0.40
	100	616	128	2.42	0.60	1.49	0.48
						1.56	0.50
						1.53	0.49

^a upper row: depth at which $^{234}\text{Th} / ^{238}\text{U}$ equilibrium is reached; lower row: constant assumed lower boundary at 100 m depth

^b upper row: 50 m depth; lower row: 150 m depth

^c at 32 m depth

^d at 90 m depth

^e row 1 (approach ED/150): ^{234}Th flux based on equilibrium depth, POC / ^{234}Th ratio from 150 m; row 2 (approach 100/150): ^{234}Th flux based on assumed 100 m depth boundary of export layer, POC / ^{234}Th ratio from 150 m; row 3 (approach ED/ED): ^{234}Th flux based on equilibrium depth, POC / ^{234}Th ratio linearly interpolated to the equilibrium depth between 50 m and 150 m; row 4 (approach 100/100): ^{234}Th flux based on assumed 100 m depth boundary of export layer, POC / ^{234}Th ratio linearly interpolated to 100 m depth between 50 m and 150 m.

Table 5. Particulate organic carbon and particulate nitrogen concentrations ($\mu\text{g L}^{-1}$) and molar C/N ratios in the particulate organic matter associated with small (0.7 – 53 μm) and large (> 53 μm) SAPS-collected particles. Uncertainties are given as one propagated standard deviation (1SD).

Station	Site	Depth (m)	0.7-53 μm						> 53 μm					
			PN	PN 1SD	POC	POC 1SD	molar C:N	C/N 1SD	PN	PN 1SD	POC	POC 1SD	molar C:N	C/N 1SD
808	N-Ref	32	3.79	0.12	22.6	0.66	6.95	0.30	0.19	0.06	1.00	0.36	6.19	2.96
803	N-Ref	150	0.71	0.02	4.53	0.17	7.39	0.35	0.13	0.02	0.86	0.10	7.99	1.54
1039	N-Slope	50	6.14	0.14	30.17	2.43	5.74	0.48	0.44	0.18	2.21	0.80	5.86	3.20
885	N-Slope	150	0.94	0.01	5.44	0.37	6.79	0.47	0.22	0.04	1.33	0.35	7.07	2.26
840	Summit	50	3.01	0.02	16.51	0.83	6.4	0.32	0.39	0.13	2.51	0.59	7.49	3.06
840	Summit	90	0.79	0.01	6.16	0.08	9.08	0.16	0.25	0.02	1.58	0.34	7.24	1.66
1002	W-Slope	50	6.29	0.16	30.75	6.07	5.71	1.14	0.33	0.12	1.58	0.49	5.63	2.69
875	W-Slope	150	0.59	0.01	4.43	0.52	8.8	1.04	0.07	0.02	0.45	0.13	7.90	3.21
1029	E-Slope	50	2.24	0.07	21.04	2.87	10.97	1.54	0.20	0.06	1.02	0.28	5.96	2.42
858	E-Slope	150	1.27	0.02	5.57	0.52	5.11	0.48	0.11	0.02	0.67	0.17	7.12	2.22
999	S-Slope	50	0.97	0.08	6.72	0.13	8.06	0.68	0.15	0.07	0.80	0.28	6.44	3.76
896	S-Slope	150	0.47	0.01	2.87	0.09	7.08	0.27	0.12	0.02	0.77	0.09	7.46	1.52
1048	S-Ref	50	0.61	0.04	5.19	0.12	9.88	0.69	0.08	0.03	0.45	0.11	6.76	3.03
1048	S-Ref	150	0.71	0.02	5.79	0.07	9.54	0.29	0.07	0.02	0.41	0.1	6.54	2.46

Table 6. Inventories of 'excess' dissolved molecular oxygen (DO), thickness of the excess layer, and maximum DO concentrations in the subsurface DO peaks at the bottom of the surface mixed layer.

Station	Site	Excess DO inventory (g m ⁻²)	Integral height (m)	Max. DO (mg L ⁻¹)
801	N-Ref	76.44	17.9	195.45
803	N-Ref	99.32	13.9	199.41
808	N-Ref	93.79	11.9	199.84
885	N-Slope	136.10	24.8	206.10
902	N-Slope	129.09	13.9	199.83
905	N-Slope	112.86	20.8	199.14
911	N-Slope	56.45	9.9	197.94
891	NW-Slope	370.80	28.8	206.33
920	NW-Slope	200.23	25.0	199.79
875	W-Slope	91.42	8.9	197.12
903	W-Slope	130.84	15.9	201.08
840	Summit	142.39	17.9	196.90
844	Summit	106.58	19.8	197.98
858	E-Slope	80.30	25.9	198.31
882	SW-Slope	100.34	20.8	199.90
895	SE-Slope	60.97	8.9	194.98
896	S-Slope	95.37	12.9	198.00